Novel acoustic method provides first detailed measurements of sediment concentration structure within submarine turbidity currents

S. M. Simmons[1], M. Azpiroz-Zabala[2], M. J. B. Cartigny[3], M. A. Clare[4], C. Cooper[5], D. R. Parsons[1], E. L. Pope[3], E. J. Sumner[6], and P. J. Talling[3]

[1]Energy and Environment Institute, University of Hull, Hull, HU6 7RX, U.K.

[2] Faculty of Civil Engineering and Geosciences, 2628 CN Delft University, The Netherlands.

[3] Departments of Earth Sciences and Geography, University of Durham, Durham DH1 3LE, U.K.

[4]National Oceanography Centre, Southampton, European Way, Southampton SO14 3ZH, U.K.

[5]formerly at Chevron Energy Technology Company, 6001 Bollinger Canyon Road, San Ramon, CA 94583, U.S.A.

[6]School of Ocean and Earth Sciences, University of Southampton, European Way Southampton SO14 3ZH, U.K.

Corresponding author: Steve Simmons (s.simmons@hull.ac.uk)

Key Points:

- First high-resolution measurements of the sediment concentration and velocity structure for multiple oceanic turbidity currents.
- Flow duration and sediment volume are strongly bimodal, and some flows are sustained for 5-10 days.
- All flows are mainly dilute (< 10 g/L), but some flows have brief (~15 min) initial period of coarser-grained or denser flow near the bed.

Abstract

Turbidity currents transport prodigious volumes of sediment to the deep-sea. But there are very few direct measurements from oceanic turbidity currents, ensuring they are poorly understood. Recent studies have used acoustic Doppler current profilers (ADCPs) to measure velocity profiles of turbidity currents. However, there were no detailed measurements of sediment concentration, which is a critical parameter because it provides the driving force, and debate centers on whether flows are dilute or dense. Here we provide the most detailed measurements yet of sediment concentration in turbidity currents via a new method using dual-frequency acoustic backscatter ADCP data. Backscatter intensity depends on size and concentration of sediment, and we disentangle these effects. This approach is used to document the internal structure of turbidity currents in Congo Canyon. Flow duration is bimodal, and some flows last for 5-10 days. All flows are mainly dilute (< 10 g/l), although faster flows contain a short-lived initial period of coarser-grained or higher-concentration flow within a few meters of the bed. The body of these flows tends towards a maximum speed of 0.8-1 m/s, which may indicate an equilibrium in which flow speeds suspend available sediment. Average sediment concentration and flow thickness determine the gravitational driving force, which we then compared to average velocities. This comparison suggests surprisingly low friction values, comparable to or less than those of major rivers. This new approach therefore provides fundamental insights into one of the major sediment transport processes on Earth.

Plain Language Summary

Seafloor-hugging flows of sediment-laden water, called turbidity currents, transport large volumes of sediment to the deep-sea and pose a hazard to seafloor infrastructure such as

pipelines and telecommunication cables. However, these flows remain poorly understood because of the limited field data available and the difficulty of measuring sediment concentration. It is sediment concentration that drives the flows, and this information is critical to modelers who seek to understand how fast and how far the flows are capable of running out along the seafloor. Recent field studies of turbidity currents have used acoustic flow-meters that measure flow velocity through vertical profiles above the sea bed. These instruments also record the magnitude of the sound reflected by the moving particles within the flow. This magnitude is related to both the concentration and grain size of the sediment. We take this information and determine the sediment concentration of ten flows at 2,000 m water depth in the Congo Canyon, offshore West Africa. Our results indicate that sediment concentrations are very dilute in most (but not all) of the flow, and we discuss potential uncertainties in these sediment concentrations. We show how the retarding force of friction is lower than expected, meaning that current flow models are likely to underestimate how fast and far the flows runout.

1. Introduction

Seafloor-hugging flows of sediment called turbidity currents flush a large amount of sediment through submarine canyons, thereby forming some of the largest sediment accumulations on our planet (called submarine fans; Bouma et al., 2012). These often-powerful flows can run out for hundreds or even thousands of kilometers (Piper et al., 1999; Talling et al., 2007). Turbidity currents play an important role in global transfer of organic carbon (Galy et al., 2007), and diversity and functioning of seafloor ecosystems (Canals et al., 2006). Turbidity currents also pose a major hazard to expensive offshore pipelines, and tele-communication cable networks that carry the vast majority of global data traffic (Carter et al., 2014). Their sedimentary deposits host valuable oil and gas reservoirs in many locations, and form unusually thick rock-sequences worldwide that record Earth history (Nilsen et al., 2008).

Compared to the other major processes that move sediment across our planet, such as terrestrial river systems, there are very few direct measurements from turbidity currents (Talling et al., 2014). This is due to their location, episodic nature, and ability to damage moorings and instruments placed in their path (Sequeiros et al., 2019). We are aware of less than ten sites worldwide where their internal velocity structure has been measured (e.g. Hughes Clarke et al. (2016); Khripounoff et al. (2012); Liu et al. (2012); Xu et al. (2004); Xu et al. (2010)). Turbidity currents are thus relatively poorly understood; with much of this understanding based on laboratory-scale experiments, analysis of their deposits, and numerical or theoretical models.

Advances in monitoring technology are now allowing turbidity currents to be monitored in action (e.g. Hughes Clarke, 2016; Azpiroz-Zabala et al., 2017; Paull et al., 2018; Hage et al., 2019). Typically, these studies use acoustic Doppler current profilers (ADCPs), which use the Doppler-shift in acoustic energy scattered from sediment particles to determine flow velocities. However, there is also a compelling need to measure the sediment concentration and hence excess density of the flow; it is this excess density that drives the turbidity current down slope. Measurements of sediment concentration are necessary to understand the basic nature and behavior of turbidity currents. This includes whether the flow is fully turbulent and dilute or driven by dense near-bed layers with marked different behavior (Kuenen and Migliorini, 1950; Talling et al., 2012; Paull et al., 2018), predictions of flow velocity (Bowen et al., 1984), whether flow is sub-critical or supercritical (Kostic and Parker, 2006), damping of turbulence (Baas et al., (2009); Cantero et al., (2012); Eggenhuisen et al. (2017)), impact forces on seabed infrastructure

(Clare et al., 2017), or rates of sediment and organic carbon transfer to the deep sea (Azpiroz-Zabala et al., 2017), and efficiency of transfer from river mouths (Galy et al., 2007).

Here we outline a novel method for calculating sediment concentration, which uses acoustic backscatter from dual-frequency ADCPs. The intensity of acoustic backscatter is strongly dependent on both the size and concentration of sediment grains (Thorne and Hanes, 2002), and these two competing effects on backscatter must therefore be disentangled.

We go on to demonstrate how this method can help to understand turbidity currents using ADCP data collected in 2009-10 from the upper Congo Canyon offshore West Africa. These are the highest frequency (5 second) ADCP measurements yet published for turbidity currents (Cooper et al., 2013, 2016; Azpiroz-Zabala et al., 2017). They have peak velocities of up to 2.8 m/s, and some flows lasted for 5-10 days (Cooper et al., 2013, 2016). This flow duration was surprising because it is far longer than previously measured oceanic turbidity currents in other locations (Azpiroz-Zabala et al., 2017).

Azpiroz-Zabala et al. (2017) provided a detailed analysis of just one of these flows, using the same dual-frequency acoustic method outlined here to constrain sediment concentrations. This analysis showed that a single flow comprised a self-sustaining frontal part (termed a frontal cell) that ran away from a slower-moving body and tail. It was proposed that this difference in speed led to stretching of the flow, which could thus explain why flows were so prolonged (Azpiroz-Zabala et al., 2017). Here we analyze 10 different turbidity currents from the same location, and thus analyse a much wider range of flow structures. This comparison between multiple flows allows us to identify three different types of turbidity currents in the Congo Canyon for the first time.

1.1. Aims

The first aim is to describe the detailed methodology used to directly measure the sediment concentration structure of turbidity currents, using dual frequency acoustic measurements. We discuss the key assumptions and uncertainties behind this method, and potential artefacts. This includes estimating the change in sediment concentration that would arise from an error in the median grain size in suspension that is used in the inversion, although this model assume that the grain size distribution does not vary with height in the flow. This helps to understand the level of confidence that can be placed in these new sediment concentration measurements. We conclude with suggestions for how uncertainties can be reduced or quantified by further work.

The second aim is to demonstrate how this new approach can help to understand the basic structure and behavior of turbidity currents, using the ADCP data set from the upper Congo Canyon. We identify three distinct types of flow structure, and seek to understand: (i) their origin, (ii) why flow duration is strongly bimodal, (iii) why the body of many different flows has a similar maximum velocity, (iv) the influence of internal tides on turbidity currents, and (v) friction coefficients that determine how gravitational driving force is related to flow speed. We conclude by comparing sediment transport rates and volumes in these turbidity currents with those in the River Congo, to understand efficiency of sediment (and organic carbon) transfer from river to deep-sea.

2. Congo Submarine Canyon

The Congo Canyon extends for almost 800 km from the mouth of the Congo River to water depths of over 5000 m (Figure 1a; Babonneau et al., 2002, 2010). The canyon has become cut deeply into the shelf and slope by the action of the sediment flows. Turbidity currents flowing down the canyon have regularly broken seafloor telecommunication cables (Heezen et al. 1964). Pioneering work obtained measurements of flow velocity at individual heights above the bed, using current meters that measure velocity at a single point (Khripounoff et al., 2003; Vangriesheim et al. 2009). Khripounoff et al. (2003) reported a flow speed of 1.21 m/s, at a height of 120 meters above the bed, in a water depth of 4,000 m. Vangriesheim et al. (2009) reported maximum flow speeds of 0.43 m/s and 0.76 m/s at heights of 60 m above the bed in water depths of 3420 m and 4050 m respectively, and transit (frontal) speeds of up to 3.5 m/s between moorings located several hundred kilometers apart.

3. Instrumentation and Data Overview

Here we analyse ADCP data from two moorings at ~2,000m water depth in the upper Congo Canyon, recorded from December 2009 to March 2010 (Figure 1a; Lucapa site of Cooper et al., 2013). A 300 kHz ADCP was suspended from the first mooring at a height of 82 m above the canyon floor, and a 75 kHz ADCP was suspended from a second mooring at a height of 220 m.

The second mooring was located 700 m down-canyon from the first mooring, downslope of a sinuous bend (Figure 1b; Cooper et al., 2013, 2016; Azpiroz-Zabala et al., 2017).

3.1. Overview of acoustic Doppler current profilers

ADCPs transmit acoustic sound-pulses into the water column and receive sound scattered back towards the instrument by material suspended in the water column. The 300 kHz and 75 kHz instruments used in this study have four transducers set at 20° to the vertical, and at 90° to each other, which generate narrow beam widths of ~4° over a seabed footprint diameter of 60 m (300 kHz) and 160 m (75 kHz). The instruments calculate flow velocity at different vertical intervals (bins) above the bed by determining the Doppler shift of the received signal along the axis of the four beams. By combining velocities from multiple beams, with heading and tilt measurements, the ADCPs resolve earth-referenced three-dimensional velocity components through a vertical profile. For this deployment, the 300 kHz and 75 kHz ADCPs acquired data using a bin size of 2 m and 4 m respectively. Velocity profiles were recorded every 5 seconds for the 300 kHz ADCP, and 6 seconds for the 75 kHz ADCP.

ADCPs also record the magnitude of the acoustic backscatter at each of the bins, which is a function of both the concentration and grain size(s) of the suspended sediment (Thorne and Hanes, 2002). Importantly, the size of grains can have a stronger influence on acoustic backscatter than the sediment concentration. This means that the competing effects of sediment grain-size and concentration need to be disentangled, in order to measure sediment concentration.

The acoustic backscatter strength from a particular bin also depends on the amount of acoustic energy that has been lost in the distance between the source and that bin. Acoustic backscatter from a particular bin thus depends on how acoustic energy is dissipated cumulatively in preceding bins. The way in which backscatter signal at one bin depends on other bins also complicates the inversion of acoustic backscatter for sediment concentration or grain size.

3.2. Side-lobe interference

The four beams of both ADCPs are slanted at 20° to the vertical and pick up off-axis reflections (side-lobe interference) from the stronger acoustic target of the seabed. In most applications these strong reflections would dominate the acoustic backscatter from suspended sediment, thus reducing the accuracy of measurements within the ~6% of the profiled water column immediately above of the seabed. However, for the 300 kHz instrument in this study, we argue that the data within this lower water column region is mostly reliable during the flow events, due to the high backscatter magnitude from relatively dense concentrations near the seabed (See Figure S1 for explanation). We therefore include velocity data and backscatter data in our analysis, but denote the vertical extent of the sidelobe region where velocities and concentrations results are plotted. Additionally, sidelobe interference can sometimes extend further from the bed. For example, when the ADCP is not located in the center of the flat channel, some of the beams will pick up off-axis reflections from the adjacent steep canyon wall.

The 300 kHz ADCP (at a height of 82 m) was located above the center of the canyon floor (Figures 1b & 1c; Cooper et al., 2013), and has a sidelobe interference region that extends to ~5 m above the bed. The 75 kHz ADCP was located closer to the canyon's side-wall, and it was thus unable to resolve velocity components and record accurate backscatter data in the lower 40 m of flow (Figure S2). However, bed-echo magnitude recovered by this 75 kHz ADCP, from its backscatter record, still plays a key role in our inversion method.

3.3. Data description and definition of turbidity current events

Periods of increased (> 0.6 m/s) flow speeds and higher backscatter, denoted in red at the top of Figure 2, are referred to as Events 1 to 10. Above this threshold, the events are clearly demarked from the observed internal tides, which are typically < 0.14 m/s. The increased water column backscatter during these 10 events is accompanied by attenuation of the strong bed-echo, which is caused by scattering and absorption of sound by suspended sediment in the water column. This bed-echo attenuation can be seen in Figure 2c, which shows echo intensity values averaged across the four beams at bin number 41. Attenuation of the bed-echo is particularly severe at the beginning of Event 8, and during part of Event 9, with the bed echo intensity value dropping to the level of the system noise. The maximum velocity value in each measured velocity profile was then defined. The average of these maximum velocities was calculated over time periods of 50 s (10 successive profiles at 5 s intervals) (Figure 2d). Concurrent increases in water column backscatter, bed-echo attenuation, and maximum flow velocity (Figure 2b-to-d) are observed during the events. Faster flows (> 1 m/s maximum profile velocity observed) that are sustained for several days (Events 1, 4, 5, 8, 9 and 10) have higher levels of backscatter and bed-echo attenuation. Shorter and slower (< 1 m/s maximum profile velocity observed) flows (Events 2, 3, 6 and 7) are related to lower levels of water-column backscatter and lower bed-echo attenuation.

4. Novel Acoustic Method for Sediment Concentration and Grain-Size

We now describe in detail the original dual-frequency acoustic backscatter inversion method that determines the concentration of suspended sediment from 300 kHz and 75 kHz ADCP data, first described in Azpiroz-Zabala et al. (2017). We employ the explicit inversion method of Lee and Hanes (1996), and perform iterative steps to determine a concentration profile that matches the measured bed echo attenuation for a particular grain size distribution. The use of multiple frequencies also provides constraints on grain size(s) in suspension, albeit assuming that the entire sediment suspension at any one time (i.e. within each ADCP-profile) comprises a single grain size distribution. Here we assume a single (log-normal) grain size distribution characterizes each vertical profile, and track how that log-normal grain-size distribution changes through time. In supplementary material, we compare this log-normal grain size distribution to an inversion based on just a single grain size. Such simplification is necessary due to a lack of direct measurements of grain size variability, and a limited number of different ADCP frequencies. However, the mean grain-size in turbidity currents most likely increases towards the seabed, and each part of the flow contains a range of grain sizes, rather than a constant grain size distribution. We therefore also provide a method for determining where sediment concentrations and grain sizes in the flow deviate most markedly from inversion results based on uniform grain-size distributions.

We outline the method (Figure 3) using the data acquired during Event 4 in 2010 (Figure 2). This moderately powerful event was chosen as it persists for several days, and because data are not degraded by the excessive sediment attenuation, causing low signal-to-noise ratios near the bed (Figure 2b). Figure 3a shows values of echo intensity averaged over the four beams of the 300 kHz ADCP.

4.1 Steps 1-4: Preparing ADCP profile data for inversion

4.1.1 Step 1 - converting raw backscatter data to a linear scale and removing noise

We now outline the series of steps used to derive sediment concentration and grain size from the ADCP backscatter data (also see Supplementary Figure 3). First, we converted the raw echo intensity data, E (RSSI), to linear backscatter counts, V, for all beams using (Gostiaux and van Haren, 2010):

$$V = \sqrt{10^{K_c E/10} - 10^{K_c N/10}} \quad (1)$$

K_c is a measured constant for each of the four transducers (i.e. values are supplied for Teledyne RDI instruments). N is the noise level for each transducer channel, determined as the average of the raw backscatter within regions of data where sediment attenuation was judged to have reduced the backscatter signal from water column material to zero. This equation recasts the raw backscatter data into new units that are easier to deal with during subsequent calculations, and subtracts the electronic noise component of the signal. Removing the noise in this manner helps reduce the bias created by the presence of the noise, in regions of the flow with a poor signal-to-noise ratio, and is a modification from the earlier version of the inversion method (Azpiroz-Zabala et al., 2017).

4.1.2. Step 2 - selecting beam by compass heading to ensure a consistent range to the bed

As the orientation of the ADCP changes during the deployment, individual ADCP beams may encounter the canyon's steep walls. ADCP data is thus filtered to avoid those orientations where a beam is directed towards the canyon sidewall. Strong echoes from the seabed are mostly present in bins numbers 40 and 41 in the 300 kHz ADCP backscatter, but higher magnitude reflections from either a bedform crest or canyon sidewall also become apparent in bin 39 at certain orientations. Figure 3b shows backscatter values at bin 39 for each of the four beams, as a function of the compass heading, for 9 days before the first event. The peaks in backscatter (that are offset by 90°) record the orientations in which each beam ensonified the steep side-wall. To prevent the bed echo from the canyon sidewall affecting the inversion process, data from a single beam were selected for processing - based on the heading during the event at that time. The range of headings that were used to select the beam are denoted in Figure 3b.

4.1.3. Step 3 – averaging successive profiles

The backscattered signal from suspended sediment particles has random phase, and multiple samples of the same concentration and grain size will produce a distribution of magnitude values (Thorne and Hanes, 2002). The root-mean square of a number of samples is typically calculated to reduce the standard error of the recorded backscatter values, albeit at the expense of temporal resolution. We calculated the root-mean-square value, V_{rms}, of 100 consecutive profiles collected over a period of 500 s for each profile that was inverted.

4.1.4. Step 4 - calculating attenuation in strength of the bed-echo (A_{bed})

We need to determine the decrease in strength (attenuation) of the bed-echo magnitude at 300 kHz for steps 5-10 of the method, where the measured attenuation is compared to that predicted from our water-column sediment concentration profile (see Thorne et al., 1995). The bed-echo attenuation throughout the turbidity current was calculated as the ratio of the backscatter in bin 41 during the event, to the backscatter in the same bin of the same beam at the same compass heading (see step 2) prior to the event. Figure 3c shows the bed-echo attenuation values (A_{bed}) for the duration of Event 4 in 2010. The bed attenuation of the lower-frequency 75 kHz ADCP is also shown, and was similarly derived using bin 55. The values of bed-echo attenuation are expressed in dB and are derived via:

$$A_{\mathrm{bed}} = 20log_{10}\left(\frac{V_{\mathrm{event}}}{V_{\mathrm{clear\ water}}}\right) \tag{2}$$

4.2. Solving the acoustic inversion problem

The mass concentration of suspended sediment within a bin, $M(r)$, is defined by the following relationship (Thorne and Hurther, 2014):

$$M(r) = \left(\frac{V_{\mathrm{rms}}(r)\varphi(r)r}{K_{\mathrm{t}}K_{\mathrm{s}}(r)}\right)^2 e^{4(\alpha_{\mathrm{w}}r+\alpha_{\mathrm{s}}(r))} \tag{3}$$

where:

- r is the distance of the bin from the ADCP transducer,
- V_{rms} (r) is the backscatter magnitude,
- $\varphi(r)$ is a correction for the transducer's near-field (Downing et al., 1995),
- K_{t} is a constant that describes the sensitivity of the individual transducer and receiver electronics, and its value is specific to a particular ADCP's hardware unit,
- K_{s} is related to the scattering properties of the sediment in suspension and is a function of the particle grain type and size relative to the acoustic frequency (see figure 3d)
- α_{w} is the sound attenuation due to the properties of the water. Here it is calculated using the formula of Francois and Garrison (1982a,b) as 0.0066 Nepers/m, using a mean water temperature of 3.7 °C, water depth of 1924 m, a pH of 8, and salinity of 35 ppt,
- α_{s} is the sound attenuation due to suspended sediment.

The sediment concentration, $M(r)$, within a bin thus depends on measured backscatter at that bin, V_{rms}, distance to the ADCP (r) together with a seawater attenuation constant, α_{w}, a near-field correction, $\varphi(r)$, an ADCP-hardware specific constant, K_{t}, and an attenuation parameter, α_{s}, that is itself a function of sediment concentration. The range, r, is divided into discrete units corresponding to the bin size of 2.13 m along the direction of the acoustic beams which are inclined at 20° to the vertical and correspond to a 2.0 m vertical bin spacing through the water column.

Solving Equation 3 is non-trivial as the sediment attenuation expression, $\alpha_{\mathrm{s}}(r)$, is itself a function of $M(r)$:

$$\alpha_S(r) = \int_0^r \xi(r) M(r) dr \tag{4}$$

where the sediment attenuation coefficient, $\xi(r)$, is a function of the particle type and size relative to the acoustic frequency. Implicit and explicit inversion methods have been developed to solve Equations (3) and (4) (see Thorne and Hanes, 2002). We employ the explicit equations of Lee and Hanes (1996) with a model of grain size suspension that assumes uniform grain size distribution throughout the profiling range. This assumed model removes the requirement of knowledge of the unknown ADCP transducer calibration constants, K_{t}, as the explicit inversion of Lee and Hanes (1996) simplifies to (Thorne and Hanes, 2002):

$$M(r) = \frac{\beta(r)^2}{\beta_{\mathrm{Ref}}^2 / M_{\mathrm{Ref}} - 4\xi \int_{r_{\mathrm{Ref}}}^{r} \beta(r)^2 dr} \tag{5}$$

where

$$\beta(r) = V_{\mathrm{rms}}(r) r e^{2\alpha_{\mathrm{w}} r} \quad (6)$$

The value of $\beta(r)$ can be calculated for each bin using the measured backscatter (V_{rms}) and known constant (α_w) and known distance to the ADCP (r). However, two parameters necessary to calculate sediment concentration profiles are still unknown. M_{Ref} is a reference sediment concentration at a reference distance from the ADCP, r_{Ref}. The sediment attenuation coefficient, ξ, is a function of grain type and size.

We now provide an overview of the method to determine these two unknown parameters and by using two sets of ADCP frequencies (300 kHz and 75 kHz), thereby defining a sediment concentration profile, $M(r)$. A flow chart of the iterative method is given by Figure S3.

4.3. Steps 5-10: Iterative calculation of the sediment concentration profile

4.3.1. Step 5 – define how ξ varies with median grain size and acoustic frequency (figure 3d)

The sediment attenuation coefficient, ξ, was first derived as the sum of acoustic scattering and viscous absorption expressions for a model grain size distribution with a range of D_{50} value. The acoustic scattering component was evaluated by first calculating the scattering cross-section, χ, using the heuristic expression of Moate and Thorne (2012), which was developed as a generic expression for sands of varying mineralogy and is described by:

$$\chi = \rho \frac{0.09(ka)^4}{1380 + 560(ka)^2 + 150(ka)^4} \quad (7)$$

where k is the wave number, a is particle radius, and ρ is sediment density which was assumed to be 2650 kg/m^3. For a grain size distribution, the ensemble scattering cross section for all particle radii in the distribution was calculated as (Thorne and Hurther, 2014):

$$\chi_e = \frac{\int_0^\infty an(a)da \int_0^\infty a^2\chi(ka)n(a)da}{\int_0^\infty a^3 n(a)da} \tag{8}$$

where $n(a)$ is the number of particles in each size fraction. The mean particle size of the distribution, a_0, was defined for the grain size distribution as

$$a_0 = \int_0^\infty an(a)da \tag{9}$$

The scattering attenuation coefficient was then calculated as (Thorne and Hurther, 2014):

$$\xi_{scattering} = \frac{3\chi_e}{4\rho a_0} \tag{10}$$

The ensemble viscous absorption component, $\xi_{viscous}$, was integrated across all volume fractions, $\varepsilon(a)$, using Urick's (1948) formulae:

$$\xi_{viscous} = \varepsilon(a)\left(\frac{k(\sigma-1)^2}{2}\left[\frac{s}{s^2+(\sigma+\delta)^2}\right]\right) \tag{11}$$

with

$$\delta = \frac{1}{2}\left[1+\frac{9}{2\Omega a}\right], \quad s = \frac{9}{4\Omega a}\left[1+\frac{1}{\Omega a}\right], \quad \sigma = \rho/\rho_0, \quad \Omega = \sqrt{\omega/2\upsilon}$$

where ρ_0 is the density of the ambient fluid, ω is the angular frequency of the pressure wave, and υ is the kinematic viscosity of water which was calculated as 1.52 × 10^{-6} m^2/s for a water temperature of 3.7 °C.

Log-normal grain size distributions are common in the marine environment (Soulsby, 1997) and appear to be similar to the grain size distributions of samples from two cores obtained in the channel near the mooring site (see Figure S4). We therefore used the log-normal model described by Moate and Thorne (2009) for the grain size distribution:

$$n(a) = \frac{1}{a\sqrt{2\pi\zeta}} e^{-\left(log_e(a-m_0)^2\right)/2\zeta^2} \quad (12)$$

with

$$\zeta = \sqrt{log_e(\gamma_0^2 + 1)}\ , m_0 = log_e\left(a_0^2/\sqrt{a_0^2 + \gamma^2}\right), \gamma = \left(\int_0^{\infty} (a - a_0)^2 n(a) da\right)^{1/2}$$

and where the relative standard deviation is defined as $\gamma_0 = \gamma/a_0$. A value of $\gamma_0 = 1.3$ was used throughout (see Section 4.4).

The plot in Figure 3d shows derived values for the sediment attenuation coefficient, ξ, across a range of D_{50} values for different log-normal distributions and for both ADCP frequencies. For small particle sizes, the viscous absorption term dominates and reaches a peak for clay/silt particles. For diameters greater than ~200 μm, the scattering term dominates at 300 kHz, and ξ increases with diameter.

4.3.2. Step 6 - assume median grain size, and search for best M_{Ref} and concentration profile in 300 kHz data

Error accumulation is a particular problem for acoustic inversions of suspended sediment when the sediment attenuation is high (Thorne et al., 2011), as is the case with the events described herein. The reference range in Equation 5, r_{Ref}, was therefore set at the farthest range, i.e. the bed in bin number 40, to prevent the accumulation of errors beyond r_{Ref}, thus mitigating the error accumulation that would likely arise using alternative inversion approaches such as the implicit, iterative method (Thorne and Hanes, 2002). A first estimate at a value for M_{Ref} was used at the reference range, r_{Ref}, to determine a first concentration profile $M(r)$. The first value of M_{Ref} used is an estimate, as the concentration at the reference range is unknown. The next step determined the cumulative through-water attenuation of the derived mass concentration profile from the transducers to the bed (bins 1 to 39), A_{profile}, using the profile of $M(r)$:

$$A_{\mathrm{profile}} = e^{\int_0^{r_{Ref}} -4\xi M(r)dr} \qquad (13)$$

The reference mass concentration was then adjusted iteratively through the above equation set until the cumulative attenuation of the derived concentration profile matched the bed echo attenuation and in essence when the difference between the two attenuation values, $A_{\mathrm{bed}-}A_{\mathrm{profile}}$, reduced to zero, giving a final profile, $M(r)$, for a particular median grain size value.

4.3.3. Step 7 – repeat for 300 kHz data using another user-defined grain size distribution

We then start again with another user-defined uniform grain size distribution, and use the 300 kHz data. The same iterative process is used to define a value of M_{Ref} that satisfies $A_{\mathrm{bed}=}A_{\mathrm{profile}}$ and hence a plausible sediment concentration profile $M(r)$ for that particular grain size distribution. This eventually results in a series of plausible sediment concentration profiles, each for a particular grain size distribution. Calculation of these multiple sediment concentration profiles for different sediment attenuation coefficients (ξ) can be done relatively easily, because $M(r)$ is inversely proportional to ξ. This allows the concentration profile to be derived without further iteration.

4.3.4. Step 8 - calculate water-column attenuation from each concentration profile with 75 kHz data

We then took each of the family of plausible sediment concentration profiles from the 300 kHz ADCP data in steps 5 to 7, and calculated the attenuation that this concentration profile would produce through the water column for a second acoustic frequency of 75 kHz.

4.3.5. Step 9 – which grain size distributions and concentration profiles also produce the bed-echo attenuation seen in 75 kHz data

We then calculated the difference between the observed bed-echo attenuation (A_{bed}) in the 75 kHz data, and the attenuation predicted using each sediment concentration profile (A_{profile} from step 4). We identified which grain sizes (and associated sediment concentration profiles) produced the observed bed-echo attenuation in the 75 kHz data, such that $A_{\text{bed=}}A_{\text{profile}}$ for the 75 kHz data. Two median (D_{50}) grain size solutions in the range between 0.1 μm to 1000 μm are found to do this, at each individual time period within the flow (an example of the two solutions for a single profile are shown as dotted vertical lines in Figure 3e).

4.3.6. Step 10 – choosing between the two possible grain sizes and concentration profiles

The smaller of the two possible grain size distributions (Fig. 3f), with a mean D_{50} value of 12 μm compared with a mean D_{50} value of 179 μm for the second solution, is the more realistic solution based on the muddy nature of canyon floor cores obtained nearby (see Azpiroz-Zabala et al., 2017, and Figure S4). The final inversion result for Event 4 employs the mean log-normal grain size distribution throughout the event (Figure 3g).

4.4. Identifying the shape of the grain size distribution.

As a test of the inversion results, the calibration constant in Equation 3, K_t, was derived for the 300 kHz ADCP water column data for all ranges, *r*, by evaluating (Thorne and Hanes, 2002):

$$K_t = \beta K_s^{-1} M^{1/2} e^{2r\alpha_s} \tag{14}$$

where K_s is a function of the sediment type and grain size and was calculated using the heuristic formulae of Moate and Thorne (2012) for the sediment form function:

$$f = \sqrt{\rho}\,\frac{\left(1 - 0.25e^{-((x-1.5)/0.35)^2}\right)\left(1 + 0.6e^{-((x-2.9)/1.15)^2}\right)x^2}{42 + 25x^2} \tag{15}$$

The ensemble form function for each grain size distribution was calculated as:

$$f_e = \left(\frac{\int_0^\infty an(a)da \int_0^\infty a^2 f^2(ka)n(a)da}{\int_0^\infty a^3 n(a)da}\right)^{1/2} \tag{15}$$

with K_s determined by:

$$K_s = \frac{f_e}{\sqrt{\rho a_0}} \tag{16}$$

The inversion method presented in Azpiroz-Zabala et al. (2017) used a single (4.3 µm) grain size model and yielded K_t values of ~ 2 x 10^8. The actual calibration constant (K_t) for the 300 kHz

ADCP remains unknown. However, calibration of similar 300 kHz instruments by the authors suggests that the actual value of K_{t} is likely to be ~ 1.7 x 10^7 for the 2 m bin size used in the deployment. The relative standard deviation, γ_0, of the log-normal grain size distribution model was therefore varied until the derived values of K_{t} matched the expected value of 1.7 x 10^7. This generally occurred using a value of $\gamma_0 = 1.3$ which was subsequently used for all inversions. The shape of the cumulative (log-normal) grain size distribution, calculated using Equation 12 with a mean D_{50} value from the inversions, is broadly similar to grain-size distributions measured in the field (Figure S4). These grain size measurements come from eight samples in two cores, located in the channel near the mooring locations. They provide confidence that the log-normal grain size distribution used here was representative of the likely range of particle sizes in suspension.

4.5 Identifying where flow is coarser or denser than single-grain size distribution model

Here we outline a validation method that helps to identify locations in the flow where our assumption of a single grain size distribution for all heights above the seabed breaks down. This provides an indication of where the flow is both coarser and denser than the inversion results presented in step 10, although it does not provide absolute density or grain size values.

If the uniform grain size distribution assumption for a given profile is true, then the calculated value of K_{t} should remain constant throughout the range from the transducers to the bed, as the true value of K_{t} is a fixed acoustic property of the transducer. Deviations in the calculated K_t can thus result from grain sizes in the flow, which deviate from our assumed grain size distribution in each ADCP profile. If the grain-sizes are different to those assumed, then this will also affect the sediment concentration value within that bin. Therefore, these deviations in K_{t} can represent differences in both grain size and sediment concentration produced by step 10. Increasing values of K_{t} suggest that the suspension is coarser-grained that the model assumed, and has a higher concentration in the regions of increased K_{t} than the values produced in step 10. As values of K_{t} were found to remain constant higher in the water column and increase towards the bed, we define an anomaly value K_{ta} as K_{t}, for each profile, divided by the mean value of K_{t} in the upper 40 m of each profile.

The values of K_{ta} are plotted for Events 1, 9 and 10 (Figure 4) and for all 10 events (Figure S6). For Event 1, the values of K_{ta} remain relatively constant throughout the duration of the event, with only a slight increase towards the bed where the mean grain size might be expected to increase. However, the K_{ta}values for Events 9 and 10 show a much more marked order of magnitude increase within a small, restricted zone near the bed within in the very early (~15 minute) stages of the flow. This suggests that there is an increase in grain size and sediment concentration in this short initial period of near-bed flow, which is consistent with the description of a ‘frontal cell’ as described in the turbidity current model of Azprioz-Zabala et al. (2017). Much smaller increase in K_{ta} are observed near the bed in the sustained bodies of the longer flows. This indicates that there is likely a greater proportion of coarser material in the grain size distributions nearer the seafloor, as would be expected for Rouse-type sediment concentration profiles (Rouse, 1937; Eggenhuisen et al., 2019). This effect would cause the sediment attenuation coefficient to decrease with the increasing grain size near the bed (Figure 3d). The single grain size distribution model would thus cause an underestimation of concentration in the near-bed region. There are no major increases in K_{ta} within the near-bed region where sidelobe interference occurs, which suggests that backscatter magnitude is significantly greater than the sidelobe interference during the events (see Figure S1). However, if there is any sidelobe interference, then it would likely cause on over-estimation of sediment concentration within the near-bed region.

5. Results

5.1. Sediment concentration structure

The acoustic inversion method was applied to the ten turbidity current events in Figure 2. The resulting concentrations of suspended sediment (g/L) are shown in Figure 5. They were derived using a single (log-normal) grain size distribution derived for each flow, as the D_{50} values remained relatively constant for the duration of the flows. Thus, sediment concentration estimates assume that the grain size distribution does not vary both above the bed, and front to back of the flow. The median value of these log-normal grain size distributions in each different flow are given in Table 1, and they vary between 6.3 and 18 μm between flows.

Sediment concentrations decrease with height above the bed for the majority of the duration of the flows and are generally around ~50% higher than the concentrations derived using the uniform single (4.3 μm) **grain size model previously reported in Azpiroz-Zabala et al. (see Figure S5 for all events).** However, in a few locations, a higher sediment concentration is observed above an area of lower sediment concentration (green circles in Figure 5). This type of inverted density structure would be unstable, and is thus most likely an artefact. We outline two different types mechanisms by which these artefacts are likely generated.

5.1.1. Origin of artefacts

The first type of artefact tends to occur in the more powerful flows (circled in green in Figure 5). This type of artefact coincides with the thickest parts of these powerful flows, and is typically found in the region of the mixing interface with the ambient flow above the turbidity current. This type of artifact is thought to be related to backscatter from turbulent microstructure associated with gradients in either density, temperature, or salinity (Lavery et al., 2003). Similar smaller-scale artefacts occur in Event 4 (Figure 5). They have a periodicity of ~12 hours, and are most likely related to internal tides flowing in the opposite direction to the turbidity current, increasing the shear and production of turbulent microstructure.

The second type of artefact is associated with high-levels of sediment attenuation, within the near-bed regions of more powerful flows (Figure 5). This artefact type most likely results from application of a spherical spreading correction, and attenuation in the water column, to what is primarily a residual of the instrument noise signal. The ADCP was set up to reject velocity measurements when the correlation threshold dropped below 64 counts or if the ambiguity velocity was greater than 2 m/s. This tended to occur in regions where the signal-to-noise ratio was poor. For example in Events 8 and 9, the region of data blanked out by the instrument is below the blue line (Figure 5). This second type of artefact thus tends to occur below those blue lines, such as in the lower 10-20 m in the first 2.5 days of Event 8 (Figure 5).

5.2. Flow velocity structure

Faster velocities occur closer to the bed, where sediment concentrations are higher. Poor-quality velocity data were discarded by the instrument when correlation and ambiguity velocity thresholds were not met, denoted by white areas in Figure 6 for Events 8 and 9.

In Events 8, 9 and 10 there is a distinctive fast-moving zone at the beginning of the flow, close to the bed. Within an hour of the event arrival, the speed of this ‘frontal cell’ (Azpiroz-Zabala et al., 2017) declines, and the height of the velocity maximum increases. Flow thickness is highly variable, sometimes exceeding the height (82 m) of the 300 kHz ADCP for Events 8 and 9. The other prolonged flows (Events 1, 4 and 5) are thinner, with a maximum thickness of 20-40 m.

5.3. Temporal changes in other key parameters

We now describe how key parameters change through time within these flows (Table 1).

5.3.1. Flow velocity

The four flows (Events 2, 3, 6 and 7) with the slowest maximum-velocity (Figure 7a) and depth-averaged velocity (Figure 7b) are also the shortest (< 1 day) in duration. Event 2 has a double peak suggesting that two shorter flows may have merged. The remaining six flows (Events 1, 4, 5, and 8-10) are much longer, persisting for 5-10 days. The six longest duration events have a faster moving (> 1 m/s) frontal-part, and a slower moving body (~ 0.6 m/s to 1 m/s) and tail (Figures 6, 7a). However, the speed of the frontal-part is only marginally greater than the body for Events 1, 4 and 5; compared with the much faster frontal-parts of Events 8, 9 and 10 (also see Azpiroz-Zabala et al., 2017 for Event 9).

5.3.2. Flow thickness

Variation in flow thickness with time were calculated using the definition of Ellison and Turner (1959), after screening out velocities below 0.2 m/s associated with internal tides (Figure 7c). Flow thickness varies greatly for the three events with the fastest frontal-parts (Events 8, 9 and 10). For these flows, the maximum thickness occurs between one and three days after the event arrival. The other long duration flows (Events 1, 4 and 5) are thinner, with thicknesses from 20 to

40 m. The three shortest duration flows, with the slowest speeds, have a maximum thickness of only 11-17 m.

5.4.3. Sediment concentration

Figure 7d and Figure 7e show the maximum and depth-averaged sediment concentration derived from inversion of the ADCP backscatter. The trend for all flows shows an initial peak in concentration maximum (always near the bed). Maximum concentration then decays rapidly over the first day, before displaying a relatively steady concentration over several days for the longer-duration flows. The higher concentrations for Event 8 (Figure 7d), during the initial 1.5 days, are an artefact generated by poor signal-to-noise ratios.

5.4.4. Grain size

Figure 7f shows the D_{50} of the grain size distribution predicted for each period of time, using the backscatter inversion method described in the text (steps 1 to 10). The grain-size distribution remains nearly constant through time for all events, with typical mean D_{50} values of 12 μm. The higher concentration flows (Events 8, 9 and 10) show less variation in the D_{50} value.

6. DISCUSSION

6.1. Assumptions and quantifying uncertainties in sediment concentration values

Importantly, it is assumed that each vertical profile through the flow comprises a single grain size distribution. But grain sizes will almost certainly vary with height, with coarser grains concentrated closer to the bed. There will also be a range of grain sizes at each point within the flow. It is also assumed that the relationship used between sediment attenuation coefficient and grain size is accurate. The relationship used here is for isolated, spherical particles, and further work may be needed to understand whether it is valid for high (> 0.5 %) sediment concentrations, flocculated sediment with irregular shapes, and the different sediment mineralogies found in the Congo Canyon.

Ideally, we would precisely quantify uncertainties in predicted sediment concentrations, to provide precise error bars on sediment concentration estimates. This is challenging, not least because submarine flows comprise a range (distribution) of grain sizes, which varies over time (i.e. front to back of flow) and with height above the bed, whilst the dual frequency acoustic inversion method provides only an estimate of a single grain size parameter for each vertical profile. Future work may explore a wider range of grain size models to better constrain uncertainties.

However, to start to assess these uncertainties, we compare results of different median grain sizes, although they all assume grain size does not vary with height above the bed. As previously outlined, the model used in the inversions is a log normal grain size distribution, whose D_{50} (typically ~10 μm) is defined via the dual-frequency acoustic inversion for each profile, but whose standard deviation is user-defined based on grain size data from cores in Congo Canyon and the expected calibration constant, K_t, for the 300 kHz ADCP. We estimate the variation in sediment concentrations for log-normal models, with D_{50} values which vary from 3 μm to 20 μm in comparison to the mean D_{50} value of 12 μm (Figure S6) for all ten events (Table 1). This comparison helps to illustrate uncertainties in sediment concentrations that would be generated by errors in the D_{50} values derived using the dual-frequency inversion. The end-member sizes (D_{50} of 3 μm and 20 μm) represent the extremes of the median grain size range of the sediment cores (see Azpiroz-Zabala et al., 2017) and provide sediment concentrations that are -20% to

+50% of those calculated using a log-normal grain size distribution with a D_{50} of 12 μm. However, these percentage-ranges do not include any effects due to grain size variations with height above the bed.

Our new method can more easily demonstrate where the turbidity current has grain-sizes or sediment concentrations that deviate from those predicted by a grain-size distribution model, and whether the flow was coarser or higher concentration in these locations. This is done by mapping out changes in a constant K_{ta} that should be uniform for a particular ADCP instrument (Section 4.5, Figure 4). Further work is required to quantify how variations in K_{ta} map to expected increases in grain size closer to the bed, and how an increase in mean grain size impacts near-bed sediment concentrations, which we expect to be higher than currently reported. Such future work is important because underestimation of near-bed sediment concentration would result in lower driving forces, and underestimation of friction coefficients. For example, a 1-m-thick near-bed layer with sediment concentration of 80 g/L would provide the same amount of sediment driving the flow, as an overlying 80-m-think layer with a sediment concentration of 1 g/L. Calculated friction coefficients (C_f) are then linearly proportional to that driving force (CH in Equation 17).

6.2. What can we learn about turbidity currents from this Congo Canyon dataset?

6.2.1. Dense or dilute flows?

Previous debate has centered on whether turbidity currents are entirely dilute, or develop high (> 9 %) concentration layers near their base (Middleton, 1967; Lowe, 1982; Kneller and Branney, 1995; Shanmugam, 1996; Talling et al., 2012; Paull et al., 2018). ADCP data shown here imply that the vast majority of these turbidity currents were particularly dilute, with concentrations of ~10 g/L to ~0.1 g/L (0.38% to 0.0038 % by volume). There is greater uncertainty in the concentrations derived from ADCP data within 3-4 meters of the bed, due to side-lobe interference. However, in one subset of flows (Events 8, 9 and 10) there is a short-lived period (20-30 mins) in which sediment sizes and concentrations are elevated within a few meters of the bed (Figures 4 and 5). This period of elevated grain size and concentration may indicate the presence of a dense near-bed layer.

6.2.2. Three flow types

Azpiroz-Zabala et al. (2017) only considered a single flow (Event 9) in detail. Here we analyse the detailed structure of 10 different flows, which allows us to recognise three flow types.

Type 1a: Prolonged and well developed frontal cell (Events 8, 9 and 10). The first type of sustained (5-6 day) flow was described previously by Azpiroz-Zabala et al. (2017). The frontal part of this flow type comprises a short-lived (20-30 minute) period with particularly fast velocities. This faster-moving zone was termed the frontal cell by Azpiroz-Zabala et al. (2017), and it runs away from the trailing body and tail. Azpiroz-Zabala et al. (2017) suggest that this causes pronounced flow stretching. The trailing body is well-developed with maximum flow speeds of 0.8-1 m/s sustained for several days (Figure 7a). Maximum velocities are located within 3-4 m of the seabed imaged by the ADCP, in the first 10-15 minutes of the flow (Azpiroz-Zabala et al., 2017; Figure 7a). The dual-frequency acoustic inversion suggests that much coarser grains or higher sediment concentrations occur in the basal 3-7m than at higher elevations, during these first 10-15 minutes of flow (Azpiroz-Zabala et al., 2017; Figure 4, Events 9). Type 1a flows are the most powerful events and have a well-developed frontal cell, which contains a brief period of coarse-grained or high concentration flow at the bed (Figure 4a). Their thickness can exceed 70 m (Fig 7b).

Type 1b: Prolonged but poorly developed frontal cell (Events 1, 4 and 5). This type of flow is also prolonged for 5-10 days, and has a well-developed body with velocities of 0.8-1 m/s for multiple days. However, it has a much weaker frontal cell than Type 1a flows, and frontal cell velocities are only slightly higher than those of the trailing body (Figure 7a). Type 1B flows lack the coarser-grained or denser period of flow seen at the start of the Type 1a flows (Figure S7).

Type 2: Shorter duration and weaker (Events 2, 3, 6 and 7). Flow duration is strongly bimodal, and Type 2 flows have a much shorter duration of ~1 day (Figure 7a). Type 2 flows are much thinner (< 17 m; Figure 7c) than Type 1 flows, and Type 2 flows are also slower moving (<1 m/s). Type 2 flows also lack a frontal zone of coarser-grained or denser flow, at least within parts of the flow imaged by the ADCPs. Type 2 flows lack the sustained trailing body seen in the Type 1 flows, such that maximum velocity tend to decrease consistently from the flow front (Figure 7a).

6.2.3. Why is flow duration strongly bimodal?

A striking observation is that flow duration appears bimodal. Flows last for either 5-10 days (Events 1, 4, 5, 8, 9 and 10), or ~1 day (Events 2, 3, 6 and 7). This bimodality suggests that the observed turbidity currents tend towards two distinct states. The faster-moving flow fronts and higher sediment concentrations that tend to be associated with the more powerful flows (see Table 1) suggests that there may be a bed sediment entrainment threshold above which the flow body enters a steady, equilibrium state that can be sustained for several days. However, flows from the same source area may stretch to different degrees because of differences in grain sizes or trigger mechanisms, or there may be differences in distance to the source of these flows. Further work is needed to distinguish between these different hypotheses.

6.2.4. Why is body velocity maximum so consistent (0.8-0.9 m/s)?

A second notable observation is that both Type 1a and 1b flows have a prolonged body whose maximum velocity of 0.8-1 m/s is broadly similar (Figure 7a). This is despite these flows having highly variable flow thicknesses (Figure 7c). This may indicate that flows have achieved a type of equilibrium state, so that this maximum body velocity remains constant for long periods.

The height of the velocity maximum provides insights into whether flows contains a fast and dense near-bed layer (c.f. Paull et al., 2018). The velocity maximum is located close to the bed during the initial part (frontal cell) of Type-1 flows, which may be driven by a dense near-bed layer. However, the velocity maximum is located well above the bed during later parts of Type-1 events, and throughout Type 1b or Type 2 events. This may suggest such flow is dilute and fully turbulent, and lacks a fast and dense near-bed layer of the type described by Paull et al. (2018).

6.2.5. Effects of internal tides on turbidity currents

Several of the turbidity currents described here from the Congo Canyon were affected by internal tides, which can travel at (up- and down-canyon) speeds of up to 0.15 m/s. This interaction is mostly clearly seen during Event 4 (Figure 8), when periodic internal tides at 50 m to 80 m above the bed (Figure 8c) appear to correspond with changes in internal flow structure. Upward vertical movement within the flow (Figure 8b) in the ~30 m above the bed coincides with the end of the down-canyon tide and decreases in the velocity maximum (Figure 8d) are observed during the up-canyon tide, suggesting that the tides strongly influence mixing within the body of the flow.

6.2.6. Relationship between gravitational driving force, flow velocity and total friction

Direct measurements of sediment concentration allow us to quantify the friction experienced by submarine flows for the first time, by comparing gravitational driving force and flow speed. Previously, friction coefficients were estimated typically from small-scale laboratory experiments, or by using friction coefficients for large rivers (Parker et al., 1986; Konsoer et al., 2013). The relationship between a turbidity current's gravitational driving force ($RCgHS$), vertically-averaged flow velocity (U), and friction coefficient (C_f) is defined using a modified Chezy equation (Konsoer et al., 2013):

$$C_f = \frac{RCgHS}{U^2} \tag{17}$$

where R is the submerged specific gravity (1.65), C is the depth averaged sediment concentration, g is the gravitational acceleration (9.81 m/s^2), H is the flow depth, S is the slope (0.007), U is the depth average velocity. C_f is the sum of the bottom and interface friction of the flow. Depth averaged values of U,H and C are estimated via the integral relations of Ellison and Turner (1959). This type of Chezy equation has long been applied to rivers, and it assumes that friction is proportional to the square of velocity. There is a linear trend between U^2 and driving force ($RCgHS$) for the data amalgamated from all ten flows (Figure 9) which indicates a friction coefficient (C_f) of 0.0031. Figure S8 shows the regressions for each of the ten events, with friction coefficient values in the range 0.0024 to 0.0043. If we assume uncertainties of -20% to 50% that are based on a comparison of log-normal distributions with D_{50} values between 3 μm and 20 μm (Figure S6), these friction coefficients vary from 0.0019 to 0.0065.

Friction coefficients of ~0.0031 are surprisingly low. The friction coefficient at the bed (C_{fb}) for turbidity currents was previously assumed to be similar to those of large rivers (0.002 to 0.005; Konsoer et al., 2013). However, turbidity currents were thought to have higher total friction coefficients (C_f) than rivers, as mixing with seawater causes additional friction along their upper surface (C_{fi}), which should further increase the overall friction.

We therefore go on to estimate the friction coefficient along the upper surface of the flow, following entrainment relation of Parker et al. (1987), which expresses the friction on the top of the flow as a function of the Richardson number (Ri):

$$C_{fi} = \frac{0.0075}{\sqrt{1 + 718Ri^{2.4}}}(1 + 0.5Ri) \tag{18}$$

where;

$$Ri = \frac{RCgH}{U^2} \tag{19}$$

The results indicate that only ~0.001 of the ~0.003 (0.0024 to 0.0043) overall friction is associated from mixing at the top interface of the turbidity currents. The ratio of bed and top interface friction is also surprisingly constant (Fig. 7i,j), given that these friction values are related to very different processes (Middleton 1993). Only in the frontal part of the flow does significant variation occur in the ratio of upper and lower boundary friction (fig. 7i,j), but care should be taken with the acoustic inversion results in these areas of higher sediment concentration or grain size (as suggested by K_{ta} values in Fig. 4) near the flow front.

These first direct measurements for deep-sea turbidity currents suggest that the overall friction coefficients are lower than past estimates, implying that models underestimated velocity of turbidity currents by up to ~100%. The low friction value could be explained by the fact the large roughness elements, such as dunes, have not been reported in the Congo Canyon (Babonneau et al., 2010), whilst they dominate bed roughness in most large rivers. The fine-grained sediments of the channel cores (Figure S4) also suggest that the channel bed is likely to be hydraulically smooth with reduced friction. Kneller et al. (2016) have argued that slow-moving turbidity carrying fine particles have a stable and stratified shear layer along their upper interface with reduced mixing. This effect would provide an additional explanation for the low friction coefficients.

It is also notable that flows with average U^2 values greater than 1 m^2/s^2 tend to deviate from this linear regression line (Fig. 9). During the faster-moving regions of flow, increases in the value of K_{ta} (Fig. 4) suggests that either the friction coefficient reduces for faster-moving flows, or that the log-normal grain size distribution assumption used in the inversion begins to break down in the few meters above the bed. This latter effect is likely due to the suspension of coarser material with a lower sediment attenuation coefficient, which would cause an underestimation of the suspended sediment concentration in our single grain size distribution model. This effect is particularly pronounced within the faster-moving frontal cells of the more powerful flows (Fig.4, Azpiroz-Zabala et al., 2017) suggesting that a dense basal layer, consistent with previous field observations in other settings (Hughes Clarke et al., 2016; Paull et al., 2018), may exist in the early stages of these flows.

6.2.8. Sediment transport rates and total volumes

This new method for deriving sediment concentrations allows us to calculate rates and total volumes of sediment transported by turbidity currents (Table 1). The more powerful and prolonged flows individually transported 1-to-5.5 Mt of sediment, at rates of up to ~0.1-to-0.8 Mt/day (Table 1). A total of ~12 Mt of sediment was transported during this 106 day period in December-March 2010. If this rate were to be sustained, it would equate to an annual flux of 41 Mt/year. Azpiroz-Zabala et al. (2017) estimated somewhat lower transport rates of 0.10 to 0.38 Mt/day for a subset of these turbidity currents, assuming the flows comprised a single grain size of 4.3 μm. This was extrapolated to an annual flux of ~22 Mt/yr (Azpiroz-Zabala et al., 2017).

There are a number of important uncertainties in sediment transport rate estimates, notably those due to inferred grain-size distributions suspended within the flow (see Section 6.1). In particular, coarser grain sizes may lead to higher near-bed sediment concentrations near the flow front (fig. 4). These sediment fluxes and volumes may also be underestimates because they neglect near-bed sediment transport as bedload, or in dense layers within the frontal cell. Conversely, turbidity currents appear to be much more frequent between December to March than during other months (Heezen et al., 1964. This would cause sediment fluxes and annual volumes to be overestimated using data from December to March, whilst much larger flows may occur over longer time scales.

However, these annual sediment flux estimates for turbidity currents, measured at a water depth of 2 km, are broadly comparable to those of the Congo River. This suggests that sediment transfer from river mouth to deep-sea canyon is highly efficient. The Congo River is estimated to transport ~43 Mt of suspended sediment to the ocean (Milliman and Meade, 1983), although Peters (1978) infer that the lower braided part of the river may transport an additional ~150 Mt/year of coarser bedload, with bedload transport of up to ~1 Mt/day during floods.

This efficiency in sediment transfer from river mouth to deep sea has important implications for global carbon cycling (Galy et al., 2007; Azpiroz-Zabala et al., 2017), or transfer of microplastic or other pollutants from the river to deep-sea (Kane and Clare, 2019). For example, we estimate that these turbidity currents transport 1.23 to 2.05 Mt/year of organic carbon, assuming an annual sediment flux of 41 Mt/year, and a (predominantly terrestrial) organic carbon content of 3-5 % by weight based on measurements from deep-sea cores (Stetten et al., 2015). This value is higher than the organic carbon flux estimated by Azpiroz-Zabala et al. (2017), and equates to 2.9 to 4.8% of the 43 Mt of terrestrial organic carbon buried globally in the oceans each year (Schlünz and Schneider, 2000). The Congo River is one of the few major river worldwide that is currently directly connected to a submarine canyon, but such direct connections were widespread during low-stands in sea-level. Our study thus supports a view that global sediment and organic carbon transfer from river mouths to the deep-sea was highly efficient during these glacial low-stands.

7. CONCLUSIONS

This study provides the most detailed measurements yet of sediment concentrations within active oceanic turbidity currents, which are one of the volumetrically important sediment transport processes on Earth. Sediment concentration is a critical parameter for understanding what turbidity currents are, and how they behave. It provides the density contrast that drives the flow, determines whether fluid-turbulence or particle-interactions dominate flow physics, and strongly affects the impact forces on seabed infrastructure such as telecommunication cables or pipelines.

We first outline a novel method based on inversion of dual-frequency acoustic measurements. The method initially assumes that each vertical profile through the flow comprises the same grain size. We then provide a way of showing where this assumption breaks down within the flow, and thus where zones of coarser-grained or higher-concentration flow occur.

This method is used to study ten turbidity currents, which occurred over ~4 months in the upper Congo Canyon. They are the most prolonged (up to 10 days), and some of the most powerful (up to 3 m/s) turbidity currents, yet measured. Three types of flow are seen, only one of which was described previously (Azpiroz-Zabala et al., 2017). The first two types of flow are sustained for 5-10 days, whilst the third type of flow last for ~1 day. Strong bimodality in flow duration may result from where flows originate, how they stretch, or other factors. All three types of flow are mainly dilute (0.2 % to 0.002 % by volume sediment), and fine grained (D_{50} of ~10 μm) suspensions. However, the first type of prolonged flow also contains a short-lived near-bed layer at its front, which is much coarser-grained or dense than the rest of the flow. The other long duration flows are somewhat weaker and thinner, and lack this near-bed zone of coarser material or higher concentrations, which is also absent in the final type of even weaker short-duration flows. Maximum velocity in profiles through the body of the two types of prolonged flow is consistently 0.8-0.9 m/s, despite substantial variations in flow thickness. This suggests that these flows tend towards an equilibrium velocity, which is sufficient to suspend canyon-floor material. We show how internal tides in the Congo Canyon induce periodic variations in internal velocities and mixing within the turbidity currents. A comparison of gravitational driving forces and flow speeds suggests that friction coefficients are much lower than previously thought, and that bottom friction dominates friction at the top interface due to mixing. The estimated annual sediment flux via submarine turbidity currents (~41 Mt/yr) is comparable to that of the River Congo, indicating highly efficient sediment routing to the deep-ocean, which has important implications for transfer of organic carbon and pollutants (e.g. microplastics) to the deep sea. This study provides the first detailed measurements of sediment concentrations within multiple full-scale oceanic turbidity currents, which is perhaps the single most important parameter for understanding how these submarine flows work, and their role in global sediment redistribution.

Acknowledgments

We thank Chevron for access to this exceptional dataset. We also thank Jon Wood (Ocean Data Technology) and others involved in collecting data. DP and SM recognise internal funding via HEIF at the University of Hull. EP was supported by a Leverhulme Trust Early Career Fellowship (ECF-2018-267). We acknowledge funding from the Natural Environment Research Council (NERC), including the following grants: NE/P005780/1, NE/P009190/1, NE/M017540/1, NE/S009965/1, NE/L009358/1, NE/N012798/1 and NE/R015953/1. All data

supporting the results in this paper are available online through NOAA's National Centers for Environmental Information (**https://accession.nodc.noaa.gov/0209071**).

References

Azpiroz-Zabala, M., Cartigny, M.J.B., Talling, P.J., Parsons, D.R., Sumner, E.J., Clare, M.A., Simmons, S.M., Cooper, C., & Pope, E.L. (2017). Newly recognised turbidity current structure can explain prolonged flushing of submarine canyons, *Science Advances*. https://doi.org/10.1126/sciadv.1700200

Baas, J. H., Best, J. L., Peakall, J. & Wang, M. (2009). A phase diagram for turbulent, transitional and laminar clay suspension flows. Journal of Sedimentary Research. *79*(3-4), 162-183

Babonneau, N., Savoye, B., Cremer, M., & Klein, B. (2002). Morphology and architecture of the present canyon and channel system of the Zaire deep-sea fan. *Marine and Petroleum Geology*, *19*(4), 445-467. https://doi.org/10.1016/S0264-8172(02)00009-0.

Babonneau, N., Savoye, B., Cremer, M., and Bez, M. (2010). Sedimentary architrecture in meanders of a submarine channel: detailed study of the present Congo turbidite channel (Zaiango Project). *Journal of Sedimentary Research*, *80*, 852–866.

Bouma, A.H., Normark, W. R. and Barnes, N. E. (2012). Submarine Fans and Related Turbidite Systems (Springer-Verlag).

Bowen, A.J., Normark, W.R., & Piper, D.J.W. (1984). Modelling of turbidity currents on Navy Submarine Fan, California Continental Borderland. *Sedimentology*, *31*(2), 169-185. https://doi.org/10.1111/j.1365-3091.1984.tb01957.

Canals, M., Puig, P., de Madron, X. D., Heussner, S., Palanques, A., Fabres, J. (2006). Flushing submarine canyons. *Nature*, *444*, 354–357.

Cantero, M., Cantelli, A., Pirmez, C. et al. (2012). Emplacement of massive turbidites linked to extinction of turbulence in turbidity currents. Nature Geosci 5, 42–45 https://doi.org/10.1038/ngeo1320

Carter, L., Gavey, R., Talling, P.J., & Liu, J.T. (2014). Insights into submarine geohazards from breaks in subsea telecommunication cables. *Oceanography*, *27*(2), 58–67. http://dx.doi.org/10.5670/oceanog.2014.40.

Clare, M.A., Vardy, M.E., Cartigny, M.J.B., Talling, P.J., Himsworth, M.D., Dix, J.K., Harris, J.M., Whitehouse, R.J.S., and Belal, M. (2017). Direct monitoring of active geohazards: emerging geophysical tools for deep-water assessments. *Near Surface Geophysics*, *15*, 427-444.

Cooper, C., Andrieux, O., & Wood, J. (2013). Turbidity current measurements in the Congo Canyon. *Offshore Technology Conference, Houston, Texas*. http://dx.doi.org/10.4043/23992-MS

Cooper, C. Wood, J. Imran, J. Islam, A. Wright, P. Faria, R. Tati, A., & Casey, Z. (2016). Designing for turbidity currents in the Congo Canyon. OTC 26919, Offshore Technology Conference, 2-5 May, Houston, Texas.

Downing, A., Thorne, P.D., & Vincent, C.E. (1995). Backscattering from a suspension in the near field of a piston transducer. *J. Acoust. Soc. Am.*, *97*, 1614-1620. http://dx.doi.org/10.1121/1.412100

Eggenhuisen, J. T., Cartigny, M. J. B., & de Leeuw, J. (2017). Physical theory for near-bed turbulent particle suspension capacity, Earth Surf. Dynam., 5, 269–281, https://doi.org/10.5194/esurf-5-269-2017.

Eggenhuisen, J.T., Tilston, M.C., de Leeuw, J., Pohl, F. and Cartigny, M.J., 2019. Turbulent diffusion modelling of sediment in turbidity currents: An experimental validation of the Rouse approach. *The Depositional Record*.

Ellison, T. H., & Turner, J. S. (1959). Turbulent entrainment in stratified flows, *J. Fluid Mech.*, *(6)*, 423-448, DOI: 10.1017/S0022112059000738

Francois, R. E., & Garrison, G.R. (1982a). Sound absorption based on ocean measurements. PartI: Pure water and magnesium sulphate contributions. *J Acoust. Soc. Am.*, *72*(3), 896–907. http://dx.doi.org/10.1121/1.388170

Francois, R. E., & Garrison, G.R. (1982b). Sound absorption based on ocean measurements. PartII: Boric acid contribution and equation for total absorption. *J. Acoust. Soc. Am.*, *72*, 1879–1890. https://dx.doi.org/10.1121/1.388673

Galy, V. France-Lanord, C., Beyssac, O., Faure, P., Kudrass, H., and Palhol, F. (2007). Efficient organic carbon burial in the Bengal fan sustained by the Himalayan erosional system. *Nature*, *450***,** 407–410.

Gostiaux, L. & van Haren, H. (2010). Extracting meaningful information from uncalibrated backscattered echo intensity data. *J. Atmos. Oceanic Technol.*, *27*(5), 943–949.

Hage, S., Cartigny, M.J.B., Sumner, E.J., Clare, M.A., Hughes Clarke, J.E., Talling, P.J., Lintern, D.G., Simmons, S.M., Silva Jacinto, R., Vellinga, A.J., Allin, J.R., Azpiroz-Zabala, M., Gales, (2019). Direct monitoring reveals initiation of turbidity currents from extremely dilute river plumes. *Geophysical Research Letters.* https://doi.org/10.1029/2019GL084526

Heezen, B.C., Menzies, R.J., Schneider, E.D., Ewing, W.M., & Granelli, N.C.L. (1964). Congo Submarine Canyon. *AAPG Bulletin*, *48*, 1126-1149.

Hughes Clarke, J. E. (2016). First wide-angle view of channelized turbidity currents links migrating cyclic steps to flow characteristics. *Nat. Commun.* 7, 11896.

Kane, I. A., & Clare M. A., (2019). Dispersion, Accumulation, and the Ultimate Fate of Microplastics in Deep-Marine Environments: A Review and Future Directions, *Frontiers in Earth Science*, 7, DOI=10.3389/feart.2019.00080

Khripounoff, A., Vangriesheim, A., Babonneau, N., Crassous, P., Dennielou, B., & Savoye, B. (2003). Direct observation of intense turbidity current activity in the Zaire submarine valley at 4000 m water depth, *Marine Geology*, *194*(3–4), 151-158. https://doi.org/10.1016/S0025-3227(02)00677-1

Khripounoff, A. Crassous, P., Lo Bue, N., Dennielou, B., & Silva Jacinto, R. (2012). Different types of sediment gravity flows detected in the Var submarine canyon (northwestern Mediterranean Sea). *Prog. Oceanogr*. 106, 138–153.

Kneller, B.C. and Branney, M.J. (1995). Sustained high-density turbidity currents and the deposition of thick massive sands. *Sedimentology*, *42(4)*, 607-616.

Kneller, B., Nasr-Azadani, M. M., Radhakrishnan, S, & Meiburg, E. (2016). Long-range sediment transport in the world's oceans by stably stratified turbidity currents, *JGR Oceans*, https://doi.org/10.1002/2016JC011978

Konsoer, K., Zinger, J., & Parker G. (2013). Bankfull hydraulic geometry of submarine channels created by turbidity currents: Relations between bankfull channel characteristics and formative flow discharge, *J. Geophys. Res. Earth Surface, 118(1),* 216-228. https://doi.org/10.1029/2012JF002422

Kostic, S., & Parker, G. (2006). The response of turbidity currents to a canyon–fan transition: Internal hydraulic jumps and depositional signatures: Journal of Hydraulic Research, *44*, 631–653.

Kuenen, P.H., & Migliorini, C.I. (1950). Turbidity currents as a cause of graded bedding. *Journal of Geology*, *58,* 91-127.

Lavery, A.C., Schmitt, R.W., & Stanton, T.K. (2003). High-frequency acoustic scattering from turbulent oceanic microstructure: The importance of density fluctuations, *J. Acoust. Soc. Am.*, *114*(5), 2685–2697.

Lee, T. H., & Hanes, D.M. (1996). Comparison of field observations of the vertical distribution of suspended sand and its prediction by models. *J. Geophys. Res. Oceans*, *101*(C2), 2156-2022. https://doi.org/10.1029/95JC03283

Liu, J. T., Wang, Y.-H., Yang, R. J., Hsu, R. T., Kao, S.-J., Lin, H.-L., & Kuo, F. H. (2012). Cyclone-induced hyperpycnal turbidity currents in a submarine canyon. *J. Geophys. Res*. 117, C04033.Lowe, D.R. (1982). Sediment gravity flows; II, Depositional models with special reference to the deposits of high-density turbidity currents. *Journal of sedimentary research*, *52(1)*, 279-297.

Lowe, D.R., (1982). Sediment gravity flows; II, Depositional models with special reference to the deposits of high-density turbidity currents. *Journal of Sedimentary Research*. 52 (1). doi: https://doi.org/10.1306/212F7F31-2B24-11D7-8648000102C1865D

Middleton, G.V. (1967). Experiments on density and turbidity currents: III. Deposition of sediment. *Canadian Journal of Earth Sciences*, *4(3)*, 475-505.

Middleton, G.V. (1993) Sediment deposition from turbidity currents. *Annu. Rev. Earth Planet. Sci.*, *21*, 89-114.

Milliman, J.D., & Meade, R.H. (1983) World-Wide Delivery of River Sediment to the Oceans. *The Journal of Geology*. Vol. *91(1)*, 1-21

Moate, B. D., & P. D. Thorne, (2009). Measurements and inversion of acoustic scattering from suspensions having broad size distributions. *J. Acoust. Soc. Am.*126, 2905. doi: 10.1121/1.3242374

Moate, B.D., & Thorne, P.D. (2012). Interpreting acoustic backscatter from suspended sediments of different and mixed mineralogical composition. *Cont. Shelf Res.*, *46*(1), 67-82. https://doi.org/10.1016/j.csr.2011.10.007

Nilsen, T.H., Shew, R. D., Steffens, & G. S., Studlick, J. R. J. (2008). Atlas of Deep-Water Outcrops (AAPG and Shell Exploration & Production).

Parker, G., Fukushima, Y., & Pantin, H. M. (1986). Self-accelerating turbidity currents. *J. Fluid Mech.*, *171*,145-181.

Parker, G., Garcia, M. H. Fukushima, Y. & Yu, W. (1987). Experiments on turbidity currents over an erodible bed, *J. Hydraul. Res.*, 25(1), 123–147.

Paull, C.K., Talling, P.J., Maier, K., Parsons, D., Xu, J., Caress, D., Gwiazda, R., Lundsten, E., Anderson, K., Barry, J., Chaffey, M., O'Reilly, T., Rosenberger, K., Simmons, S., McCann, M., McGann, M., Kieft, B., Gales, J., Sumner, E.J., Clare, M.A., & Cartigny, M.J.B. (2018). Powerful turbidity currents driven by dense basal layers. Nature Communications, *Nat. Commun*. *9*, 4114. https://doi.org/10.1038/s41467-018-06254-6

Peters, J.J. (1978). Discharge and sand transport in the braided zone of the Zaire estuary. *Neth. J. Sea Res*. *12(3-4)*: 273-292. https://hdl.handle.net/10.1016/0077-7579(78)90031-5

Piper, D. J. W., Cochonat, P., & Morrison, M.L. (1999). The sequence of events around the epicentre of the 1929 Grand Banks earthquake: initiation of debris flows and turbidity current inferred from sidescan sonar, *Sedimentology*, *46*(1), 79-97.

Rouse, H., 1937. Modern conceptions of the mechanics of fluid turbulence. *Trans. A.S.C.E.*, 102, 463-543.

Schlünz, B. & Schneider, R. R. (2000). Transport of terrestrial organic carbon to the oceans by rivers: Re-estimating flux- and burial rates. *Int. J. Earth Sci*. 88, 599–606.

Sequeiros, O.E., Pittaluga, M.B., Frascati, A., Pirmez, C., Masson, D.G., Weaver, P., Crosby, A.R., Lazzaro, G., Botter, G. & Rimmer, J.G. (2019). How typhoons trigger turbidity currents in submarine canyons. *Scientific reports*, *9*.

Shanmugam, G., 1996. High-density turbidity currents; are they sandy debris flows?. *Journal of sedimentary research*, *66(1)*, 2-10.

Soulsby, R. (1997). Dynamics of Marine Sands (Thomas Telford, London).

Stetten, E., Baudin, F., Reyss, J.-H. Martinez, P. Charlier, K., Schnyder, J., Rabouille, C., Dennielou, B. Coston-Guarini, J. & Pruski, A. M. (2015). Organic matter characterization and distribution in sediments of the terminal lobes of the Congo deep-sea fan: Evidence for the direct influence of the Congo River. *Mar. Geol.* 369, 182–195.

Talling P. J., Wynn, R.B., Masson, D.G., Frenz, M., Cronin, B.T., Schiebel, R., Akhmetzhanov, A.M., Dallmeier-Tiessen, S., Benetti, S., Weaver, P.P.E., Georgiopoulou, A., Zühlsdorff, C., & Amy, L.A., (2007). Onset of submarine debris flow deposition far from original giant landslide, Nature, *450*, 541-544.

Talling, P.J., Masson D.G., Sumner, E.J., & Malgesini, G. (2012). Subaqueous sediment density flows: Depositional processes and deposit types. *Sedimentology*, *59*(7), 1937-2003.

Talling, P.J., Paull, C.K., and Piper, D.J.W. (2014). How are subaqueous sediment density flows triggered, what is their internal structure and how does it evolve? Direct observations from monitoring of active flows. *Earth Science Reviews*, 125, 244-287.

Thorne, P.D., & Hanes, D.M. (2002). A review of acoustic measurement of small-scale sediment processes, *Cont. Shelf Res.*, *22*, 603-622. https://doi.org/10.1016/S0278-4343(01)00101-7

Thorne, P.D., Holdaway, G.P., & Hardcastle, P.J. (1995). Constraining acoustic backscatter estimates of suspended sediment concentration profiles using the bed echo. *J. Acoust. Soc. Am.*, *98*, 2280-2288. http://dx.doi.org/10.1121/1.413342

Thorne, P.D., Hurther, D., & Moate, B.D. (2011). Acoustic inversions for measuring boundary layer suspended sediment processes, *J.Acoust.Soc.Am*. *130(3)*, 1188-1200

Thorne, P.D., & Hurther, D. (2014). An overview on the use of backscattered sound for measuring suspended particle size and concentration profiles in non-cohesive inorganic sediment transport studies, *Cont. Shelf Res.*, *73*, 97-118. https://doi.org/10.1016/j.csr.2013.10.017

Urick, R.J., (1948). The absorption of sound in suspensions of irregular particles, *J. Acoust. Soc. Am.*, *20*, 283–289. https://doi.org/10.1121/1.1906373

Vangriesheim, A., Khripounoff, A., & Crassous, P. (2009). Turbidity events observed in situ along the Congo submarine channel. *Deep-Sea Res. II*, *56*, 2208–2222. https://doi.org/10.1016/j.dsr2.2009.04.004

Xu, J. P., Noble, M. A., & Rosenfeld, L. K. (2004). In-situ measurements of velocity structure within turbidity currents. Geophys. Res. Lett. 31, L09311.

Xu, J. P., Swatzenski, P. W., Noble, M. , & Li, A.-C. (2010) Event-driven sediment flux in Hueneme and Mugu submarine canyons, southern California. *Mar. Geol*. 269, 74–88.

976 **Figures**

977

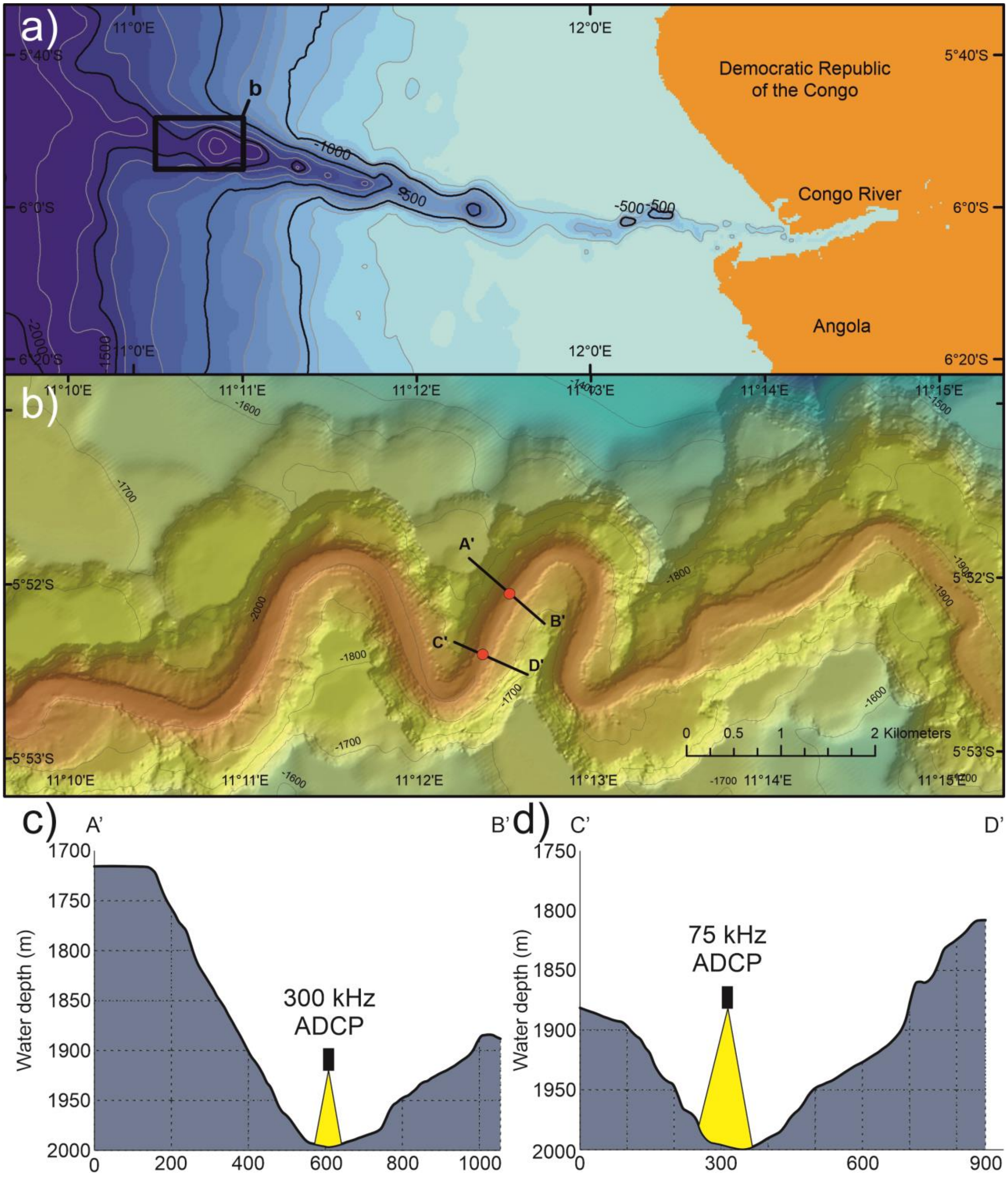

978

Figure 1. Location of turbidity current measurements in the Congo Canyon. (a) Map of the Congo Canyon showing study area (rectangle), with bathymetric contours in meters. (b) Location of mooring sites within the rectangle (Cooper et al., 2013). Bold lines indicate locations of cross-canyon profiles shown in (c) and (d) with ADCPs suspended above the canyon floor.

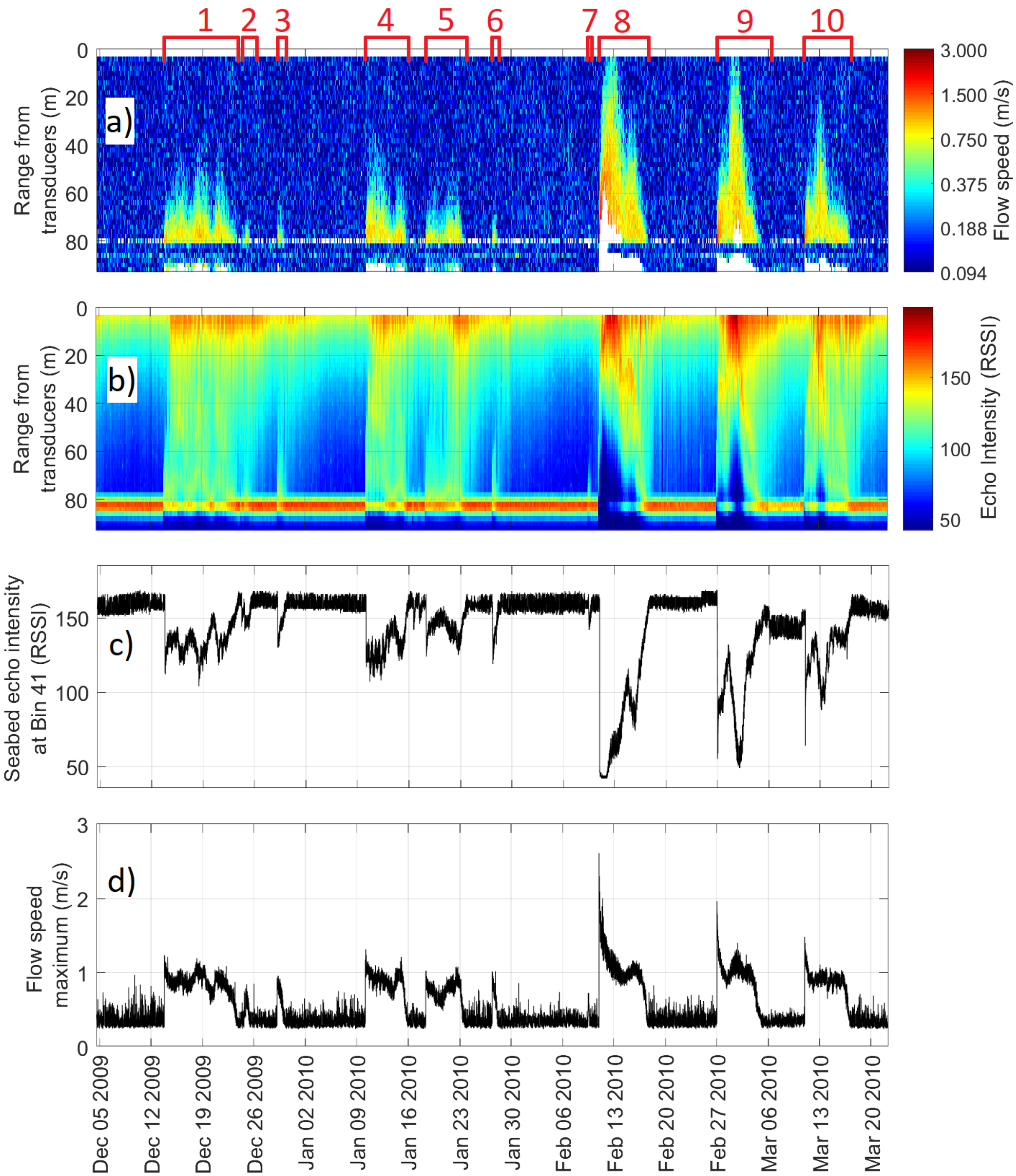

Figure 2. Backscatter and velocity data acquired by the 300 kHz ADCP in 2009-2010. Ten sediment-flow events, numbered occurred during this deployment. (a) Flow speed (m/s). (b) Raw backscatter data (RSSI) averaged across the four ADCP beams. (c) Raw backscatter in Bin

Number 41 (assumed to be the seabed) averaged across the four beams. (d) Maximum velocity (m/s) measured in each velocity profile, and then averaged over periods of 50 s.

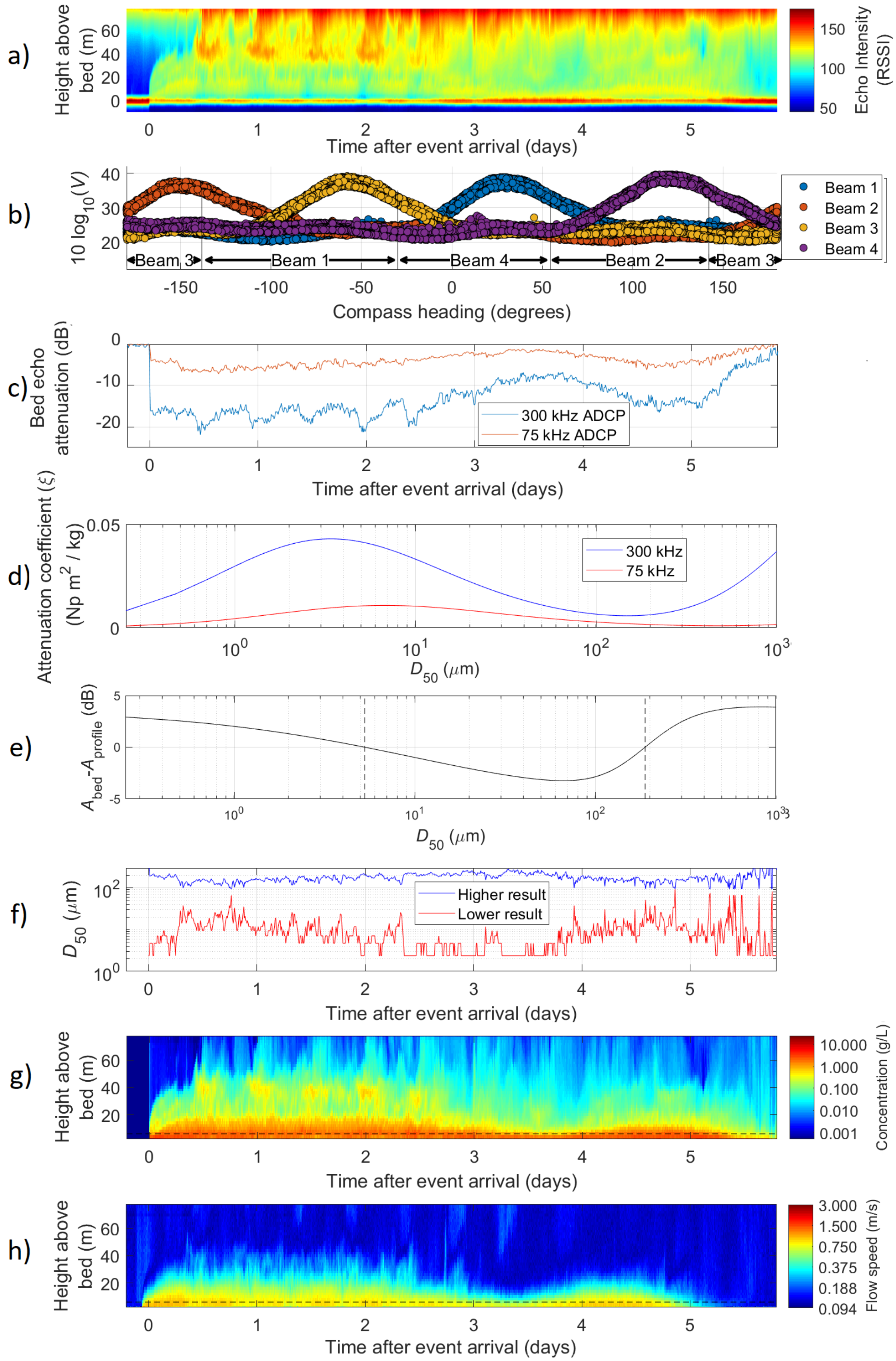

a)
Height above bed (m)
Time after event arrival (days)
Echo Intensity (RSSI)
b)
10 log10(V)
Beam 1
Beam 2
Beam 3
Beam 4
Compass heading (degrees)
c)
Bed echo attenuation (dB)
300 kHz ADCP
75 kHz ADCP
Time after event arrival (days)
d)
Attenuation coefficient (ξ) (Np m2 / kg)
300 kHz
75 kHz
D50 (μm)
e)
Abed-Aprofile (dB)
D50 (μm)
f)
D50 (μm)
Higher result
Lower result
Time after event arrival (days)
g)
Height above bed (m)
Concentration (g/L)
Time after event arrival (days)
h)
Height above bed (m)
Flow speed (m/s)
Time after event arrival (days)

990

Figure 3. Illustration of how acoustic backscatter is used to constrain sediment concentration and grain size. Parts a, c and e-g relate to data from the case study, Event 4, whereas parts b and d show data that are used for the inversion of all 10 identified events. **(a)** Raw backscatter (RSSI) averaged over the four ADCP beams during Event 4. **(b)** Relationship between the compass heading of the ADCP and backscatter magnitude in the near-bed bin before the flow events. The plot shows each of the 4 ADCP beams in a different colour. At any given ADCP orientation, one of the four beams produces much higher backscatter because it illuminates a region of higher elevation seabed. Data from each beam is thus only used in this analysis for a narrow range of compass bearings. **(c)** Amount of attenuation of the bed-echo (dB) during Event 4 for both 75 and 300 kHz ADCPs. This attenuation value is the decrease in bed echo strength during the flow, compared with the value before the flow. **(d)** Plot showing how sediment attenuation coefficient varies with D_{50} values of log-normal grain size distributions for both ADCP frequencies. **(e)** Values of $A_{bed} - A_{profile}$ for a single point in time during Event 4, with $A_{profile}$ calculated using *M(r)* profiles derived from the 300 kHz data, and A_{bed} measured using the 75 kHz data. The D_{50} of the two log-normal grain size distributions that cause A_{bed} to equal $A_{profile}$ are shown by vertical dotted lines. **(f)** Time series through Event 4, showing the the D_{50} of the two grain size distribution solutions (see part e) for Event 4, derived using backscatter from both ADCPs. **(g)** Concentration of suspended sediment for Event 4 derived using a log-normal grain size distribution with a D_{50} of µm, which does not vary through time. **(h)** Speed of Event 4 from velocity profiles averaged over 500 s. Horizontal dashed lines in parts g and h denote the extent of the near-bed sidelobe interference region.

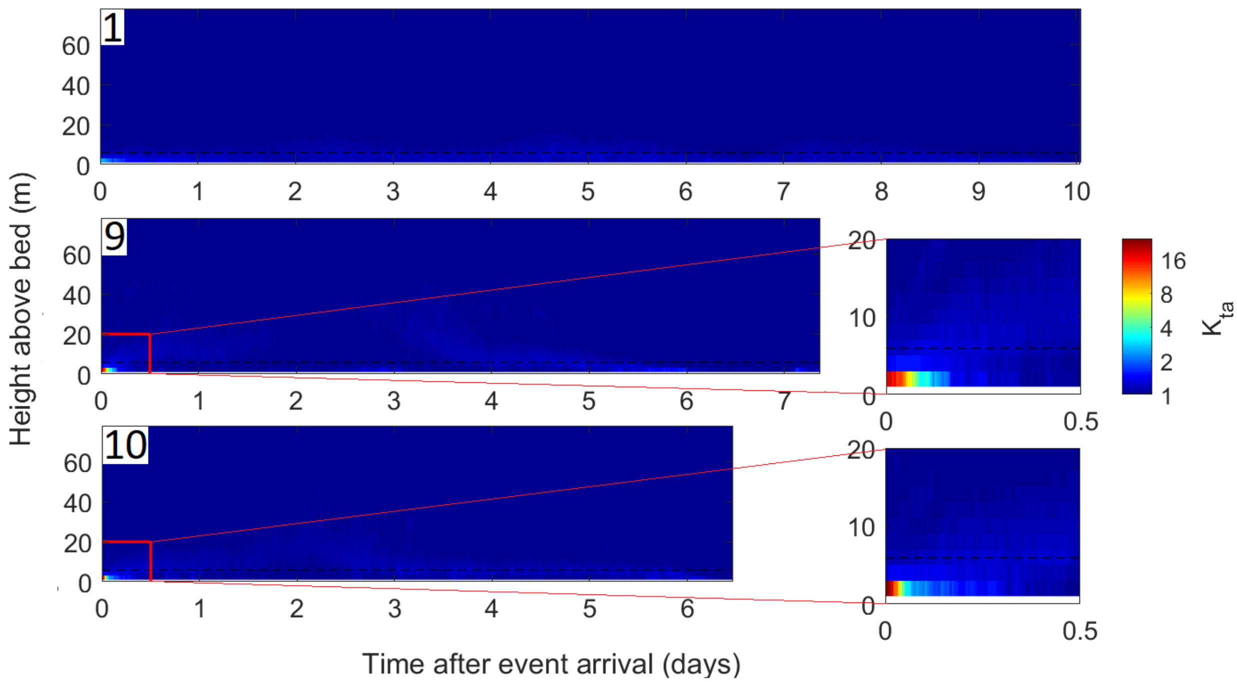

Figure 4. Derived calibration constant anomaly (K_{ta}) values for Events 1, 9 and 10. Details of the flow front are shown in more detail. Dashed lines show the potential extent of the near-bed sidelobe region. K_{ta} values should be constant for the ADCP. Variations in K_{ta} thus highlight where flow may be coarser-grained or higher-concentration than in the single grain size distribution model.

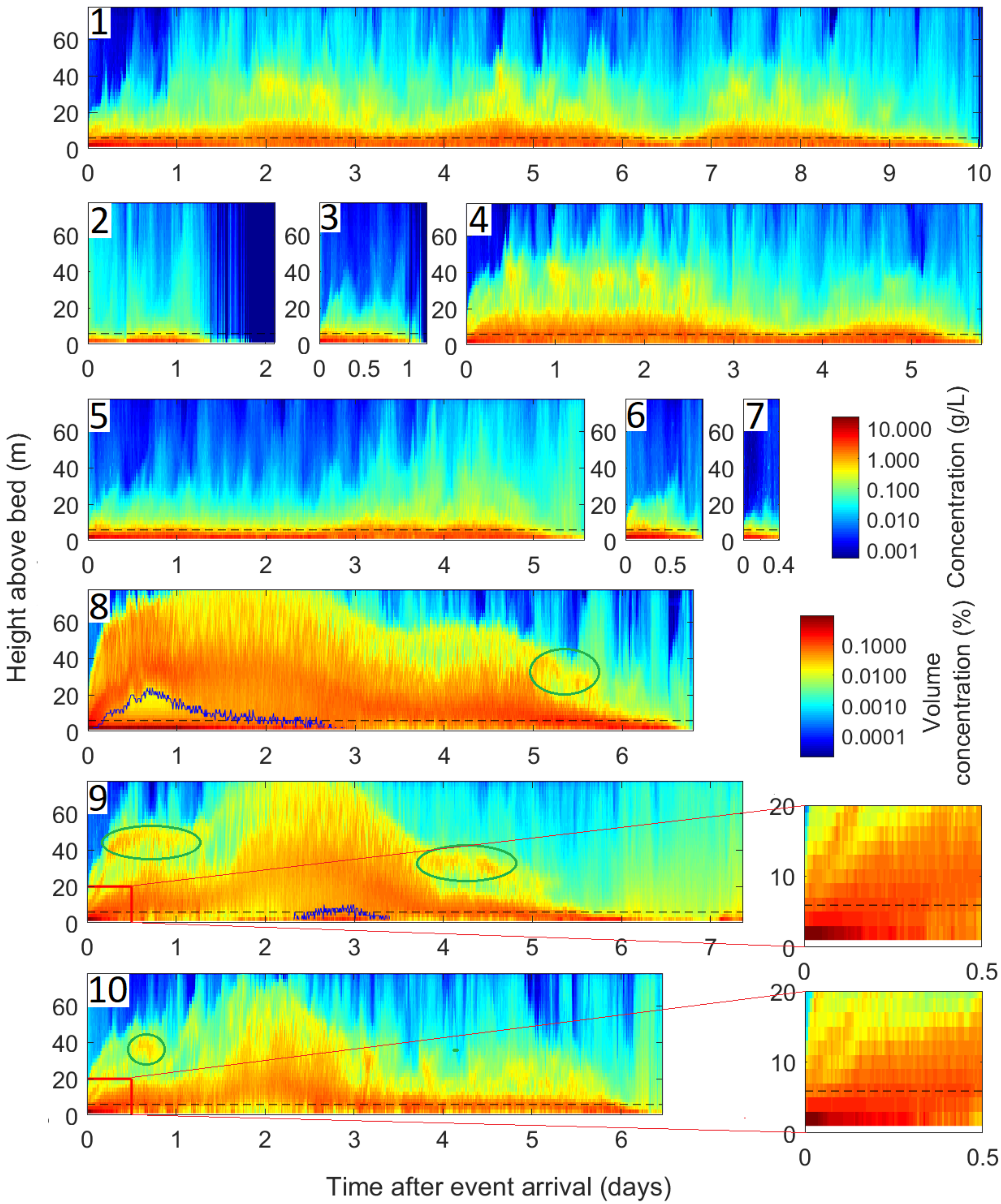
1
2
3
4
5
6
7
8
9
10
Height above bed (m)
Time after event arrival (days)
Concentration (g/L)
10.000
1.000
0.100
0.010
0.001
Volume concentration (%)
0.1000
0.0100
0.0010
0.0001

Figure 5. Sediment concentrations estimated from acoustic backscatter for Events 1 to 10, using a single grain size distribution for each event. More detailed views are provided for the frontal parts of Events 9 and 10. Horizontal dashed lines show the typical extent of the near-bed sidelobe region, calculated as ~6% of the height of the ADCP above the bed. Note meaningful data can be returned from this near-bed zone, if sediment concentrations are sufficiently high. Locations where higher sediment concentrations overly lower sediment concentrations are likely to be artefacts, with examples highlighted by the green ovals. The blue lines represent the range beyond which ADCP rejects velocity data in Events 8 and 9, due to poor signal-to-noise ratios.

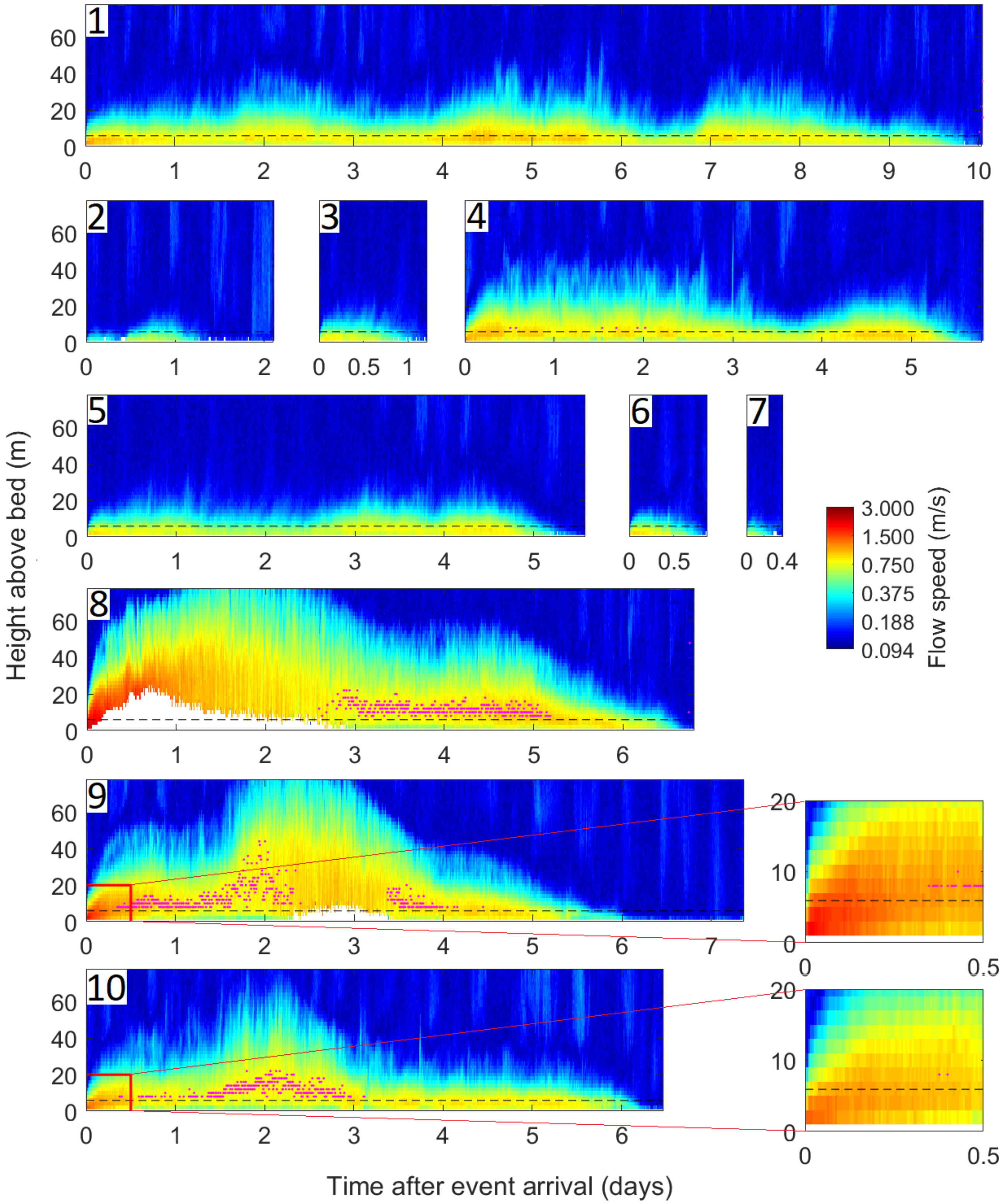

Figure 6. Velocity structure of 10 turbidity currents in the Congo Canyon. Velocities measured every 5 s by the 300 kHz ADCP, and averaged over 500 s intervals. Details of flow front shown for Events 9 and 10. Dashed lines show height that is 6% of distance from bed to ADCP, where side-lobe interference can occur,

if sediment concentrations are not sufficiently high. Purple dots show height of velocity maximum, when it can be identified confidently (i.e. it is above sidelobe interference region, and there is no major data loss due to signal-to-noise issues). Azpiroz-Zabala et al. (2017) provide a detailed analysis of Event 9.

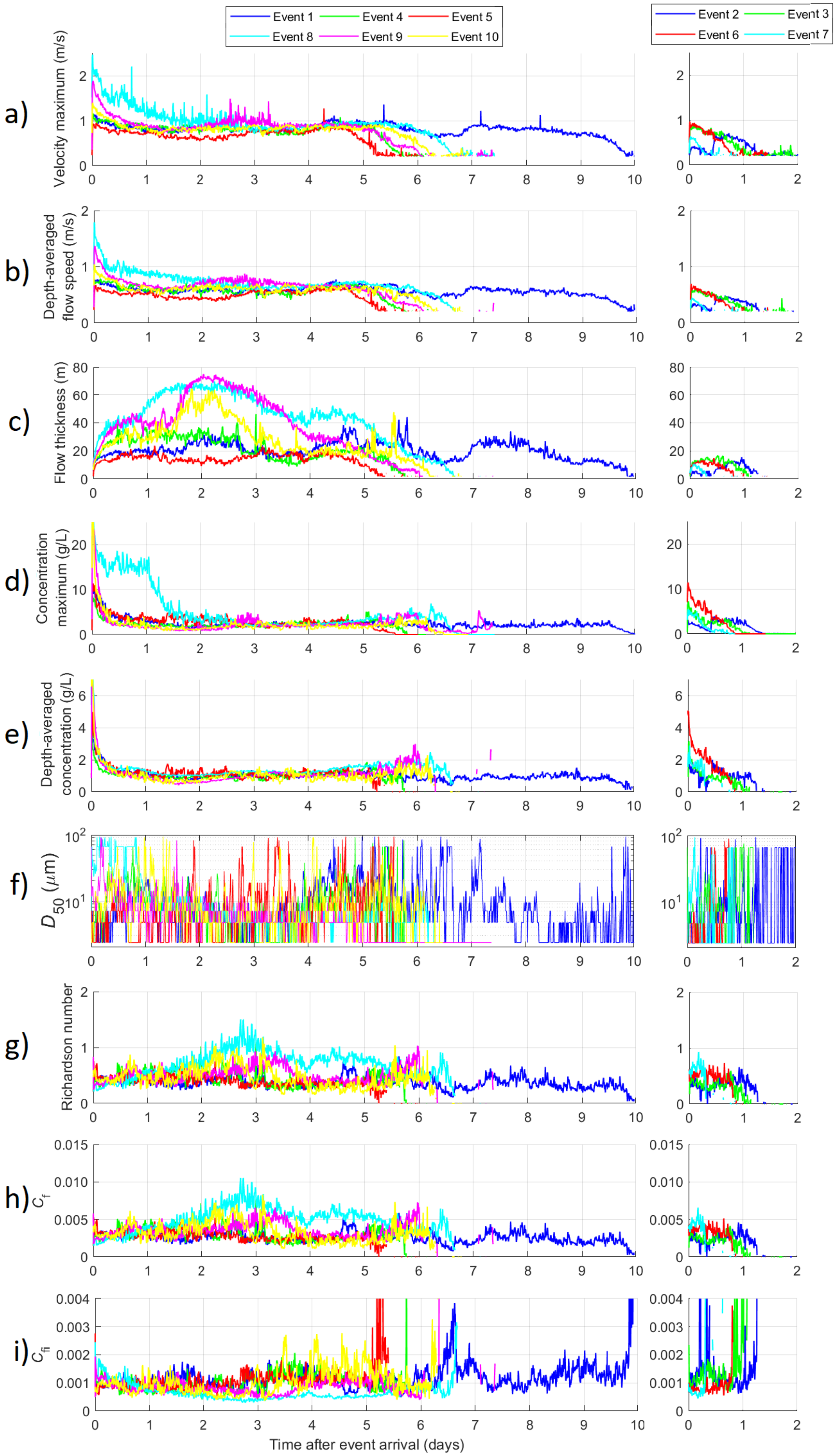
Event 1
Event 4
Event 5
Event 8
Event 9
Event 10
Event 2
Event 3
Event 6
Event 7
a)
Velocity maximum (m/s)
b)
Depth-averaged flow speed (m/s)
c)
Flow thickness (m)
d)
Concentration maximum (g/L)
e)
Depth-averaged concentration (g/L)
f)
D_{50} (μm)
g)
Richardson number
h)
C_f
i)
C_{fi}
Time after event arrival (days)

Figure 7. Variation in key parameters through time during Events 1 to 10, using data averaged over 500 s. (a) Maximum velocity (m/s). (b) Depth-averaged flow speed. (c) Flow thickness (m). (d) Maximum sediment concentration (g/L). (e) Depth-averaged concentration. (f) D_{50} of log-normal grain size distribution predicted from ADCP backscatter inversion, assuming a single grain size distribution in each profile. (g) Richardson number. (h) Friction coefficient. (i) Interface coefficient. The six most prolonged events are plotted on the left, and the four short-lived events on the right.

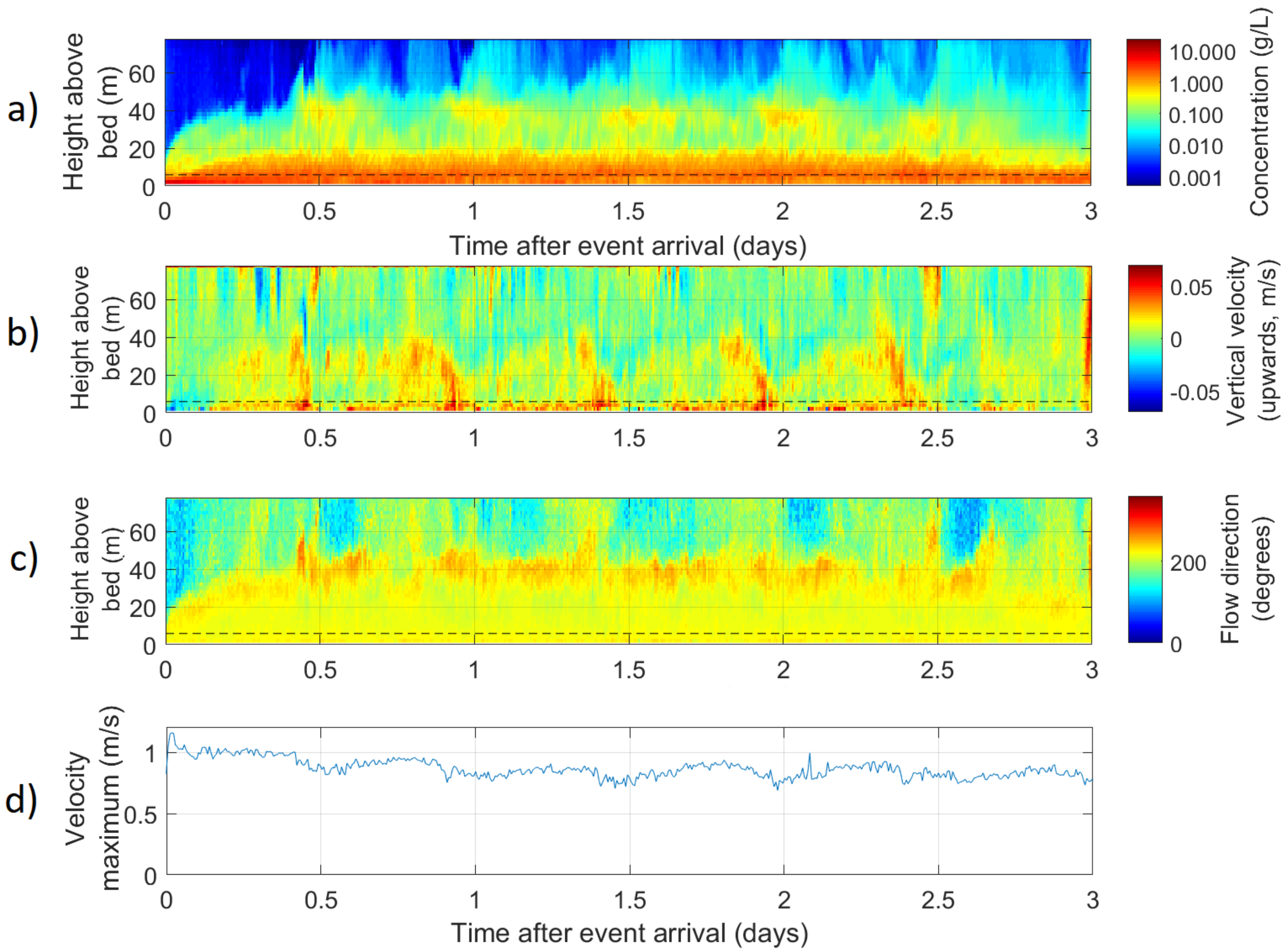

Figure 8. Plots showing the periodic (~12 hour) influence of internal tides on turbidity current Event 4 in Congo Canyon. (a) Sediment concentration structure, including artefacts most likely associated with increased micro-turbulence due to internal tides (see discussion in main text). (b) Vertical component of flow velocity. (c) Flow direction within or above the turbidity current. (d) Maximum velocity (averaged over 500 s) measured within the turbidity current.

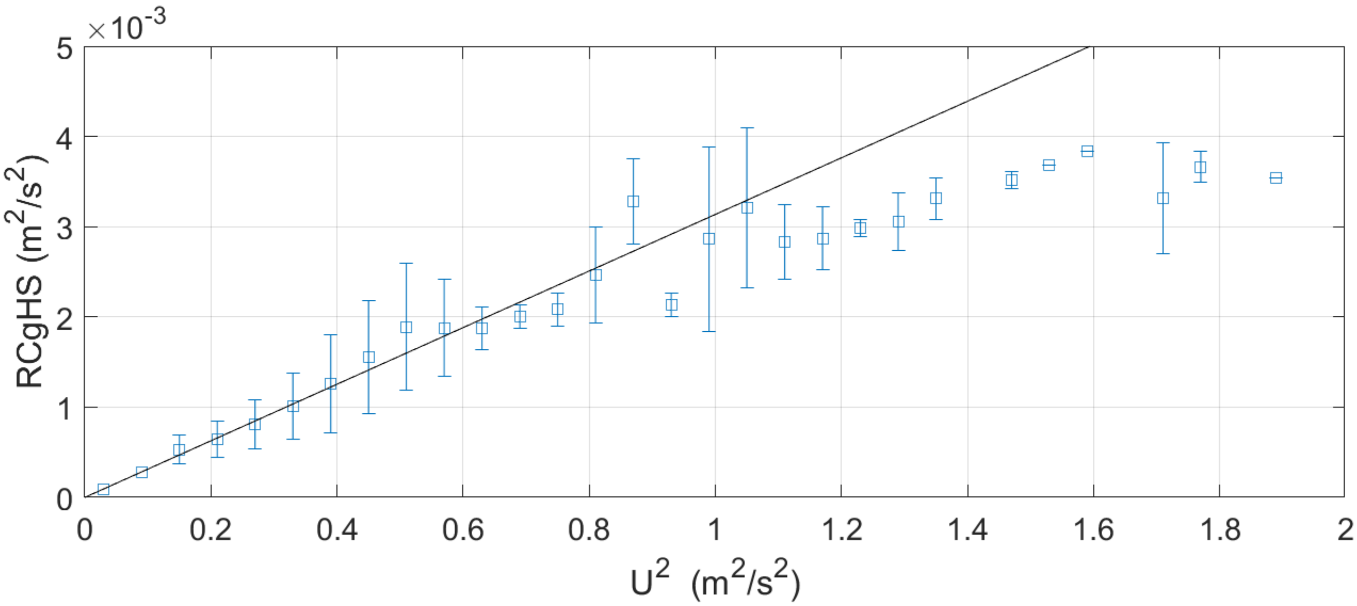

Figure 9. Regression through the origin of *RCgHS* versus U^2 to determine the friction coefficient, C_f, using data from all ten events. ADCP profiles that contain blanked areas due to poor signal-to-noise ratios are not included. Blue squares show the mean of data within each 0.06 m^2/s^2 bin and the vertical lines indicate the standard deviation of the same data.

Event	**1**	**2**	**3**	**4**	**5**	**6**	**7**	**8**	**9**	**10**
Flow duration (days)	10.1	1.0	1.0	5.5	5.2	0.7	0.41	6.6	6.3	6.3
Maximum flow thickness (m)	44.2	15.6	16.9	46.2	23.8	15.0	10.7	70.0	75.2	64.8
Maximum speed (m/s)	1.15	0.71	0.87	1.16	0.95	0.97	0.64	2.42	1.89	1.40
Maximum concentration (g/L)	10.84	3.87	7.24	8.70	11.36	11.40	5.51	29.91	24.92	29.31
Maximum concentration (%$_{vol}$)	0.40	0.14	0.27	0.32	0.42	0.43	0.20	1.12	0.94	1.10
Mean D_{50} (μm)	11.0	18.0	15.3	9.9	10.6	12.5	13.2	12.8	6.3	10.6
Sediment volume displaced (Mt)	1.063	0.022	0.028	0.783	0.314	0.036	0.006	5.531	2.763	1.415

Table 1. Flow parameters for Events 1 to 10. Velocity and suspended sediment profiles for periods of 500 s.